Directional nonclassicality of resonance fluorescence from a three-body quantum antenna via geometry-dependent frequency engineering

Ze-an Peng,[1] Guo-qing Yang,[2] Guang-ming Huang,[1] and Gao-xiang Li[1,*]

[1]*Department of Physics, Huazhong Normal University, Wuhan 430079, China*
[2]*College of Electronics and Information, Hangzhou Dianzi University, Hangzhou 310018, China*

By constructing a quantum filtering system to synthesize the spectral and spatial properties of stimulated radiation, the directionality of spectrally correlated nonclassical properties of resonance fluorescence from a three-body quantum antenna is investigated. The quantum antenna consists of three two-level quantum emitters, two of which are identical and strongly driven by an external laser field to radiate the collective resonance fluorescence with three distinct spectral components. The collective stimulated radiation is shaped by the remaining auxiliary emitter via its spontaneous emission, which is assumed to be resonant with the higher-frequency spectral component of the two identical emitters. Due to the presence of the auxiliary emitter, highly directional nonclassicality of the spectral correlations can be generated, which is the consequence of the internal interference of the source and the spatial interference of the radiation field. The electric dipole-dipole interaction between the undriven emitter and the dressed two-body radiating source plays a crucial role in breaking the rotational symmetry of nonclassical signals, which is embodied by various photon correlation functions with a frequency-resolved version for different spectral combinations. By correlating the two opposite sidebands, the frequency-resolved intensity-intensity correlation functions can signal highly directional nonclassicality, and the frequency-resolved two-mode entanglement along a specific emission direction can be tested by the frequency-resolved anomalous correlation function. While the directional nonclassical correlations between the central-frequency and the three-body collective higher-frequency components can be identified through the frequency-resolved intensity-field correlation function. These various frequency-resolved correlation functions characterize the spatial asymmetry of nonclassical properties of the collective stimulated radiation from different perspectives, including the particle properties and the quantum coherences of the filtered photons. When the three-body collective higher-frequency sidebands are correlated with the central band and the lower-frequency sideband, respectively, the schemes of using the auxiliary undriven emitter to generate optimal nonclassical correlations with well-defined directions are discussed analytically. In addition, the results obtained from the three-body quantum antenna and a dressed two-body quantum antenna are compared.

I. INTRODUCTION

The research of multiatom systems has always been one of the most fascinating fields in quantum optics, atomic and molecular physics, and condensed matter physics. Since the theories of superradiance [1,2] and subradiance [3,4], the landmarks of collective radiation theory, have been disclosed in the early days, the extensive interests in radiative characteristics of multiatom systems can be traced back to the cooperative dynamics of multiatom systems. Some of the intriguing cooperative phenomena include the interference of two-atom radiation [5], multiatom entanglement [6], collective Lamb shift [7], hyperradiance [8], birth, death, and revival of collective spontaneous emissions [9], etc. Nowadays, with the proliferation of nanophotonics technologies, one-dimensional waveguides, plasmonic structures, and metamaterials have served as powerful platforms to give prominence to the physical potential of multiatom systems [10–14]. More practically, the pragmatic value of multiatom systems has penetrated into the field of quantum information science [15,16]. Undoubtedly, the abundant phenomena occurring in multiatom systems have been refreshing our cognitions of atom-photon interactions.

Quantum antenna is a very fashionable topic about multiatom systems in recent years, which involves the design of geometrical configuration and the control of radiative properties of the arrays of quantum emitters. In terms of the geometrical configurations, current researches mainly focus on linear arrays [17–24] and two-dimensional arrays [25,26,28–30] with beautiful radiation patterns. However, even the most prototypical structure, the two-atom radiating system, can constantly bring us novel discoveries [31–36]. In the aspect of space-dependent physical signals, the direction-resolved higher-order photon correlations may provide opportunities for tailoring collective radiation effects. For instance, superradiance and subradiance were revisited recently with a renewal of interest via detecting higher-order photon correlations [18,19], and a variety of schemes of engineering photon statistics in spatial domain have also been proposed [24,33–

36]. As for the physical arrangement of quantum antennas, many collective effects are based on vacuum-mediated photon exchange in the absence of external driving fields. The main purpose is to concentrate on the desired atomic superposition states that are critical for the additional collective effects related to superradiance or subradiance. Recently, the geometrical dependence of stimulated radiation of quantum antennas driven by an external laser field has gradually attracted attention [23,24,31,32,37–39]. However, to our knowledge, only a few works have been devoted to the spectral-directional comprehensive characteristics of stimulated radiation of quantum antennas driven by a strong laser field, especially including dipole-dipole interactions. In view of the increasing popularity of the frequency-filtering techniques in recent years, especially for resonance fluorescence [40–44], more abundant physical scenarios may be discovered through jointly monitoring the spectral and directional properties of resonance fluorescence from quantum antennas driven by strong laser fields.

In this paper, by constructing a quantum filtering system to synthesize the spectral and spatial properties of stimulated radiation, we propose a theoretical scheme of generating strongly directional nonclassicality of the frequency-resolved resonance fluorescence radiated from a strongly driven three-body quantum antenna. Our main idea is to break the rotational symmetry of the nonclassicality via dipole-dipole interactions, which give rise to the internal atomic coherence effects. We find that the internal interference of the source and the spatial interference of the radiated field can produce strongly directional nonclassicality between different spectral components. In addition to the widely discussed intensity-intensity correlations, we also examine the intensity-field correlations [45–51] and the anomalous correlations [52,53] to test the frequency-resolved nonclassicality. Arguably, the concept of intensity-field correlations is a remarkable breakthrough in the development of quantum correlations, and anomalous correlations are closely related to two-mode entanglement. Our results indicate that these correlation functions can convey the information about the interference effects of internal-state and space that are required to produce the strongly directional nonclassicality.

As for the configuration design of the quantum filtering system, on the one hand, the quantum antenna is composed of three two-level electric dipolar emitters, two of which are identical and driven by a strong laser field, while the remaining one is far off-resonant with the former two for shaping the collective resonance fluorescence via its spontaneous emission. As a quantum antenna, it may be more accessible for observing directionality when the interatomic distance is comparable with the resonance wavelength [22]. In this case, the electric dipole-dipole interactions can be treated as perturbations relative to the strong laser-atom interaction. Thus the collective resonance fluorescence spectrum in our system is split into three spectral components that can be individually addressable. We further specify the transition of the undriven emitter to be resonant with the higher-frequency sideband. In this arrangement, both the spectral combination of the two opposite side-frequency components and the spectral combination of the central-frequency and the side-frequency components are involved in the three-body cooperative

photons. For these two spectral combinations, we also discuss how to use the undriven emitter to generate optimal nonclassical correlation signals with well-defined directions and the unidirectional nonclassical correlation signals in the direction of the central vertical line of the driven two-emitter axis. On the other hand, we establish the filtering dynamics by applying three single-mode quantum optical cavities to simulate three Lorentzian filters. The description is in the frame of cascaded quantum system. As we shall see, it enables us to propose the analytical approach that are also applicable to other quantum filtering systems described by the Lorentzian filtering functions.

This paper is organized as follows. In Sec. II, the quantum filtering system is introduced by deriving the master equation. In Sec. III, the quantum state of the quantum filtering system is calculated. The calculations are carried out analytically in the corresponding Hilbert space of the full system truncated at double-excitation states of the target cavity modes. In Sec. IV, we correlate different spectral components to investigate their geometry-dependent nonclassical properties. For different spectral combinations, we apply different criteria of nonclassicality of two-mode quantized fields. In addition, the results are compared with a strongly driven two-emitter system. Finally, we summarize our results in Sec. V.

II. QUANTUM FILTERING SYSTEM AND MASTER EQUATION

A. Description of the quantum filtering system

The quantum antenna we consider consists of three electric dipolar emitters, each of which is modeled by a two-level system with the ground state $|g_i\rangle$ and the excited state $|e_i\rangle$ ($i \in \{1, 2, 3\}$), separated by the transition frequency ω_i and connected by the electric dipole moment $\mathbf{d}_i$. Among them, the emitters 1 and 2 are selected to constitute the principle radiating source of resonance fluorescence, which are assumed to be identical and driven simultaneously by a monochromatic strong laser field. Their collective stimulated radiation is regulated by the remaining auxiliary undriven emitter 3 via its spontaneous emission, which is assumed to be far off-resonant with the two driven emitters. In practical terms, the frequency mismatch always needs to be considered between two nonidentical quantum dots [54–58], and this driving arrangement can be achieved, for example, by trapping the two driven emitters and the undriven emitter at an antinode and a node of a standing-wave laser field, respectively [59,60]. In some recent researches of the linear chains of identical two-level atoms, only one atom is selectively driven by an external laser field [23,24,59]. As illustrated in Fig. 1, we introduce the coordinates such that the three emitters are located at positions $\mathbf{r}_1 = (0, -r_{12}/2, 0)$, $\mathbf{r}_2 = (0, r_{12}/2, 0)$, and $\mathbf{r}_3 = (-r_3 \sin \vartheta_3 \sin \varphi_3, r_3 \sin \vartheta_3 \cos \varphi_3, r_3 \cos \vartheta_3)$, respectively. The spherical angles ϑ_3 and φ_3 will be determined by the geometrical configuration of the quantum antenna we are interested in.

The three-body cooperative dynamics is established by a common electromagnetic reservoir, which not only leads to the spontaneous decay of individual emitter, characterized by
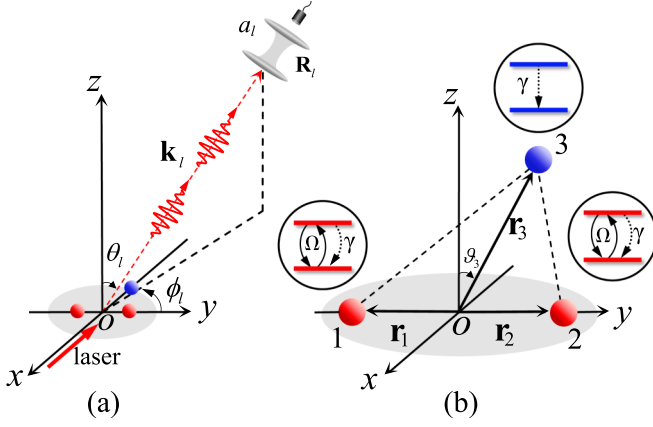
FIG. 1. (a) Geometry of the investigated quantum filtering system. Three filters are simulated by the three single-mode optical cavities described by the respective annihilation operators a_l ($l \in \{1, 2, 3\}$), each of which is equipped with a photodetector at the far-field position $\mathbf{R}_l$ (only one cavity is sketched in (a) as an example). The observation direction is determined by (θ_l, ϕ_l). (b) Geometrical structure of the three-body quantum antenna, where two identical quantum emitters (red dots), labeled by 1 and 2, respectively, are driven by a strong laser field propagating in the direction perpendicular to the y axis, i.e., $\mathbf{k}_L \perp \mathbf{r}_{12}$. The parameter ϑ_3 is the elevation angle of the position of the auxiliary undriven emitter 3 (blue dot).

the spontaneous decay rate γ_i, but also provides the electric dipole-dipole interactions via photon exchanges. The coherent and dissipative coupling rates between any two emitters i and j ($i \neq j$) are determined by the electromagnetic Green's tensor in free space [27,28]

$$
\begin{aligned}
\mathbf{G}(\mathbf{r}_i, \mathbf{r}_j, \omega_0) &= \mathbf{G}(\mathbf{r}_{ij}, \omega_0) \\
&= \frac{e^{ik_0 r_{ij}}}{4\pi k_0^2 r_{ij}^3} \Big\{ [(k_0 r_{ij})^2 + i k_0 r_{ij} - 1] \mathbb{I} \\
&\quad + [-(k_0 r_{ij})^2 - 3 i k_0 r_{ij} + 3] \frac{\mathbf{r}_{ij} \mathbf{r}_{ij}}{r_{ij}^2} \Big\},
\end{aligned} \quad (1)
$$

through the relations

$$
\Omega_{ij} = -\frac{3\pi \sqrt{\gamma_i \gamma_j}}{k_0} \hat{\mathbf{d}}_i^* \cdot \mathrm{Re}[\mathbf{G}(\mathbf{r}_i, \mathbf{r}_j, \omega_0)] \cdot \hat{\mathbf{d}}_j,
$$

$$
\gamma_{ij} = \frac{6\pi \sqrt{\gamma_i \gamma_j}}{k_0} \hat{\mathbf{d}}_i^* \cdot \mathrm{Im}[\mathbf{G}(\mathbf{r}_i, \mathbf{r}_j, \omega_0)] \cdot \hat{\mathbf{d}}_j, \quad (2)
$$

respectively. In Eq. (1), $r_{ij} = |\mathbf{r}_{ij}|$ with $\mathbf{r}_{ij} = \mathbf{r}_i - \mathbf{r}_j$ represents the inter-emitter distance, $k_0 = 2\pi/\lambda_0 = \omega_0/c$ is the wave number of the radiation fields related to the resonance wavelength λ_0 and the central frequency of the atomic transition ω_0, and $\mathbb{I}$ is the unit tensor. In Eq. (2), $\hat{\mathbf{d}}_{i(j)}$ is the unit vector of the electric dipole moment of the $i(j)$th emitter. In our system, all the electric dipole moments are oriented to be parallel to each other.

In our scheme, the quantum antenna is in the regime of strong driving. Specifically, it refers to the situation in which the Rabi frequencies of the quantum emitter-laser interactions are much larger than all the vacuum-induced rates. In this case, similar to the single-atom Mollow triplet, the two-emitter collective resonance fluorescence is well split into

three spectral components, and no significant subversion of the spectral shape caused by the electric dipole-dipole interactions arises. In order to extract different spectral components, three single-mode quantum optical cavities, described by their respective bosonic annihilation (creation) operators a_l ($a_l^\dagger$) ($l \in \{1, 2, 3\}$), are arranged at the positions $\mathbf{R}_l$ in far-field zone to filter the higher-frequency, the central-frequency, and the lower-frequency spectral components of the incident fluorescent fields with the propagation vectors $\mathbf{k}_l$, respectively. The position of each cavity can be expressed as $\mathbf{R}_l = R_l \mathbf{e}_l$ with $\mathbf{e}_l = (-\sin \theta_l \sin \phi_l, \sin \theta_l \cos \phi_l, \cos \theta_l)$. Based on the main spirit of filtering mechanism that each filter is weakly coupled with the source so that there is no back action from the filter to the source [61], in our scheme, we describe the filtering dynamics in the frame of cascaded quantum system [62–66].

B. Master equation

The dynamics of the total quantum filtering system, including the three-body quantum antenna and the target cavity modes, is governed by the master equation for the density operator ρ. In the frame rotating of the frequency of the strong driving field, the master equation has the form (setting $\hbar = 1$ throughout the paper) [67–69]

$$
\frac{d\rho}{dt} = -i[H, \rho] + \mathcal{L}_S \rho + \mathcal{L}_C \rho + \mathcal{L}_{SC} \rho, \quad (3)
$$

with the total Hamiltonian $H = H_S + H_L + H_{dd} + H_C$, where

$$
H_S = \frac{1}{2} \sum_{i=1}^3 \Delta_i S_i^z, \quad H_C = \sum_{l=1}^3 \delta_l a_l^\dagger a_l,
$$

$$
H_L = \frac{1}{2} \sum_{i=1}^2 [\Omega(\mathbf{r}_i) S_i^+ + \Omega^*(\mathbf{r}_i) S_i^-],
$$

$$
H_{dd} = \frac{1}{2} \sum_{i \neq j=1}^3 \Omega_{ij} (S_i^+ S_j^- + S_j^+ S_i^-). \quad (4)
$$

The Hamiltonians H_S and H_C represent, respectively, the free energies of the three-body quantum antenna and the cavity modes. The parameters $\Delta_i = \omega_i - \omega_L$ and $\delta_l = \nu_l - \omega_L$ are the detunings of the transition frequency ω_i of the ith emitter and the resonance frequency ν_l of the lth cavity, respectively, with respect to the driving frequency ω_L, and we have $\Delta_1 = \Delta_2 = \Delta$ for the identical emitters 1 and 2. The Hamiltonian H_L describes the semiclassical interactions between the emitters 1 and 2 with the strong classical driving field, where $\Omega(\mathbf{r}_i)$ is the Rabi frequency experienced by the ith emitter. Note that the Rabi frequency experienced by each of the driven emitters is dependent on the position vector of the emitter, for example $\Omega(\mathbf{r}_i) = \mathbf{d}_i \cdot \mathbf{E}_L e^{i(\mathbf{k}_L \cdot \mathbf{r}_i + \phi_L)}$ for running-wave driving field, where $\mathbf{E}_L$ and $\mathbf{k}_L$ are, respectively, the amplitudes and the wave vector of the driving field [60,68]. When the direction of the wave vector of the strong driving field $\mathbf{k}_L$ is perpendicular to the axis between the two identical emitters ($\mathbf{d}_1 = \mathbf{d}_2$), i.e., $\mathbf{k}_L \cdot \mathbf{r}_{12} = 0$, we can achieve the simple situation $\Omega(\mathbf{r}_1) = \Omega(\mathbf{r}_2) = \Omega$ [68]. The operator $S_i^z = |e_i\rangle\langle e_i| - |g_i\rangle\langle g_i|$ is the energy operator of the ith emitter, and $S_i^- = |g_i\rangle\langle e_i|$ and $S_i^+ = |e_i\rangle\langle g_i|$ are, respectively, the lowering and raising operators of the ith emitter. The last term of the total Hamiltonian, H_{dd},

represents all the possible coherent dipole-dipole couplings with the commutative symmetry $\Omega_{ij} = \Omega_{ji}$. The damping terms in Eq. (3) take the forms

$$\mathcal{L}_S\rho = \sum_{i,j=1}^{3} \frac{\gamma_{ij}}{2}(2S_i^- \rho S_j^+ - S_j^+ S_i^- \rho - \rho S_j^+ S_i^-),$$

$$\mathcal{L}_C\rho = \sum_{l=1}^{3} \frac{\kappa_l}{2}(2a_l \rho a_l^\dagger - a_l^\dagger a_l \rho - \rho a_l^\dagger a_l),$$

$$\mathcal{L}_{SC}\rho = -\sum_{i=1}^{3}\sum_{l=1}^{3} \sqrt{\mu\kappa_l\gamma_i}([a_l^\dagger, S_i^- \rho]e^{-ik_0 x_{il}} + \text{H.c.}). \quad (5)$$

Here the abbreviation "H.c." is the Hermitian conjugate. The first damping term, $\mathcal{L}_S\rho$, describes the internal dissipation of the quantum antenna, including the spontaneous decay of each emitter for $i = j$ with $\gamma_{ii} = \gamma_i$ and the inter-emitter dissipative dipole-dipole couplings for $i \neq j$ with the coupling rates $\gamma_{ij} = \gamma_{ji}$. The second damping term describes the decays of the cavity modes with their respective decay rates κ_l. The filtering dynamics in our system is described by the cascaded term $\mathcal{L}_{SC}$ [62–66]. It suggests that each cavity is excited by the incident fluorescent fields unidirectionally and dissipatively with the spatial phase $k_0 x_{il} = k_0|\mathbf{R}_l - \mathbf{r}_i|$ accumulated by the propagation of the radiation fields [69]. In far-field zone, we have $k_0 x_{il} \approx k_0 R_l - \mathbf{k}_l \cdot \mathbf{r}_i$. The coefficient $\sqrt{\mu\kappa_l\gamma_i}$ is the dissipative coupling rate between the ith emitter and the lth target cavity, where the parameter μ is the fraction of emission reaching the filter per decay event of the single emitter. For simplicity, we assume $\kappa_l = \kappa$ and $\gamma_i = \gamma$ in the following.

It is well known that the multipeak pattern of resonance fluorescence spectrum emerges in the regime of strong driving [67,70]. In our quantum filtering system, this condition is specified as $\Omega \gg \{\Omega_{ij}, \gamma_{ij}, \kappa, \gamma\}$. Therefore one can obtain a dressed Hilbert space of the three-body quantum antenna by diagonalizing $H_S + H_L$ into $\tilde{H}_S$, which is spaced by the dressed-state bases $\{|k\rangle\}$ with $k \in \{1, 2, \ldots, 8\}$ (see Appendix A). The eigenvalues of the dressed states allow us to recognize clearly that the separation between the center frequencies of two adjacent peaks of the resonance fluorescence spectrum of each dressed emitter is $\bar{\Omega} = \sqrt{\Delta^2 + \Omega^2}$. We further specify the transition frequency of the emitter 3 to be tuned to resonance with the higher-frequency spectral component of the collective resonance fluorescence, i.e., $\Delta_3 = \bar{\Omega}$. Therefore the three-body cooperative radiation is concentrated on this sideband. The condition of sideband resonance enables the three-body cooperative photons to participate in two different types of spectral combination simultaneously, one is the combination of the two opposite sidebands, and the other combination involves the central-frequency and the side-frequency components. In spectral domain, we aim the cavities 1, 2, and 3 at the higher-frequency, the central-frequency, and the lower-frequency components, respectively. Therefore the total electric dipole radiation operator of the source resolved by the three-cavity monitoring system can be reorganized by the dressed-state transition operators $\sigma_{kk'} = $

$|k\rangle\langle k'|$ ($k, k' \in \{1, 2, \ldots, 8\}$) as

$$\sigma_1 = \sum_{i=1}^{3} S_1^{(i)} e^{-i(k_0 R_1 - \mathbf{k}_1 \cdot \mathbf{r}_i)},$$

$$\sigma_2 = \sum_{i=1}^{2} S_2^{(i)} e^{-i(k_0 R_2 - \mathbf{k}_2 \cdot \mathbf{r}_i)},$$

$$\sigma_3 = \sum_{i=1}^{2} S_3^{(i)} e^{-i(k_0 R_3 - \mathbf{k}_3 \cdot \mathbf{r}_i)}. \quad (6)$$

Here the operator $S_l^{(i)}$ in Eq. (6) represents the weighted sum of all the possible higher-frequency ($l = 1$), the central-frequency ($l = 2$), and the lower-frequency ($l = 3$) internal-state atomic transition operators of the ith emitter through the dressed-state transition amplitudes $A_1 = c^2$, $A_2 = s^2$, $B_1 = \sqrt{2}cs$, and $B_2 = \frac{1}{\sqrt{2}}(c^2 - s^2)$ with $c, s = \sqrt{(\bar{\Omega} \pm \Delta)/2\bar{\Omega}}$. Obviously, for the condition of higher-frequency sideband resonance, we have the relation $S_1^{(3)} = S_3^-$. However, the operators σ_l ($l \in \{1, 2, 3\}$) are not only related to $A_{1,2}$ and $B_{1,2}$, but also to the following geometry factors

$$f_1(\mathbf{k}_l) = e^{i\mathbf{k}_l \cdot \mathbf{r}_1} + e^{i\mathbf{k}_l \cdot \mathbf{r}_2}, \quad l \in \{1, 2, 3\},$$

$$f_2(\mathbf{k}_l) = e^{i\mathbf{k}_l \cdot \mathbf{r}_1} - e^{i\mathbf{k}_l \cdot \mathbf{r}_2}, \quad l \in \{1, 2, 3\},$$

$$f_3(\mathbf{k}_1) = e^{i\mathbf{k}_1 \cdot \mathbf{r}_3}, \quad (7)$$

which are crucial to the spatial regulation of the radiated field. The specific expansions of σ_l have been given by Eq. (A10) in Appendix A. Hence Eq. (6) suggests that the filtered signal is the consequence of two interference effects, one involving the internal-state quantum interference in the source, i.e., the coherent superposition of atomic states, and the other involving the spatial interference of the radiated fields embodied by the geometry factors, which is present also in classical light fields.

Considering that the electric dipole-dipole interactions can be tackled as perturbations relative to the strong-driving regime when the inter-emitter distance is of the order of (even less than) the resonance wavelength, let us perform the unitary transformation via $e^{i\tilde{H}_S t/\hbar}\rho(t)e^{-i\tilde{H}_S t/\hbar}$ to extract the main resonant interactions by neglecting rapidly oscillating terms. After transforming back to the original picture, the master equation can be rewritten in terms of the dressed states as

$$\frac{d\rho}{dt} = -i[\tilde{H}_0 + \tilde{H}_I + \tilde{H}_C, \rho] + \tilde{\mathcal{L}}_S\rho + \tilde{\mathcal{L}}_C\rho + \tilde{\mathcal{L}}_{SC}\rho, \quad (8)$$

where the transformed Hamiltonians take the forms

$$\tilde{H}_0 = \hbar \sum_{k=1}^{8} \Omega_k \sigma_{kk}, \quad \tilde{H}_C = H_C,$$

$$\tilde{H}_I = \hbar\Omega_+^{(dd)}(\sigma_{24} + \sigma_{42}) - \hbar\Omega_+^{(dd)}(\sigma_{67} + \sigma_{76})$$
$$+ \hbar\Omega_-^{(dd)}(\sigma_{23} + \sigma_{32}) + \hbar\Omega_-^{(dd)}(\sigma_{57} + \sigma_{75}). \quad (9)$$

The transformed damping terms of the three-body quantum antenna can be written as $\tilde{\mathcal{L}}_S\rho = \tilde{\mathcal{L}}_{S_1}\rho + \tilde{\mathcal{L}}_{S_2}\rho + \tilde{\mathcal{L}}_{S_3}\rho$

with

$$\tilde{\mathcal{L}}_{S_1}\rho = \sum_{i,j=1}^{3} \frac{\gamma_{ij}}{2}\big(2S_1^{(i)}\rho S_1^{(j)\dagger} - S_1^{(j)\dagger}S_1^{(i)}\rho - \rho S_1^{(j)\dagger}S_1^{(i)}\big),$$

$$\tilde{\mathcal{L}}_{S_2}\rho = \sum_{i,j=1}^{2} \frac{\gamma_{ij}}{2}\big(2S_2^{(i)}\rho S_2^{(j)\dagger} - S_2^{(j)\dagger}S_2^{(i)}\rho - \rho S_2^{(j)\dagger}S_2^{(i)}\big),$$

$$\tilde{\mathcal{L}}_{S_3}\rho = \sum_{i,j=1}^{2} \frac{\gamma_{ij}}{2}\big(2S_3^{(i)}\rho S_3^{(j)\dagger} - S_3^{(j)\dagger}S_3^{(i)}\rho - \rho S_3^{(j)\dagger}S_3^{(i)}\big), \quad (10)$$

and the cascaded dissipative coupling term is transformed into a more transparent form as

$$\tilde{\mathcal{L}}_{SC}\rho = -\sqrt{\mu\kappa\gamma}\sum_{l=1}^{3}([a_l^{\dagger},\sigma_l\rho] + [\rho\sigma_l^{\dagger}, a_l]). \quad (11)$$

In the transformed master equation, the Hamiltonians $\tilde{H}_0$ and $\tilde{H}_I$ represent the free part and the interaction part of the dressed two-emitter subsystem, where the energies Ω_k have been given by Eqs. (A4)–(A6) in Appendix A, and $\Omega_{\pm}^{(dd)} = \frac{A_1}{\sqrt{2}}(\Omega_{13} \pm \Omega_{23})$. As for the damping terms, one can see that all the filtering dynamics are classified by the filtering frequency ν_l irrespective of the positions of the quantum emitters.

III. ANALYTICAL FORMALISM AND MAIN EMISSION MECHANISM

The Hamiltonian and dissipation of the quantum antenna (source) in Eqs. (9) and (10) indicate that, in the case of higher-frequency sideband resonance, the presence of the auxiliary emitter provides the atomic coherent effects for the two sets of degenerate dressed states $\{|2\rangle, |3\rangle, |4\rangle\}$ and $\{|5\rangle, |6\rangle, |7\rangle\}$ [see Eq. (A5)] with the effective coherent coupling rates $\Omega_{\pm}^{(dd)} = \frac{A_1}{\sqrt{2}}(\Omega_{13} \pm \Omega_{23})$ and the effective dissipative coupling rates $\gamma_{\pm}^{(dd)} = \frac{A_1}{2\sqrt{2}}(\gamma_{13} \pm \gamma_{23})$. In physical terms, these two sets of coupling rates are originated from the processes that the two driven emitters exchange photons collectively with the third one in phase and in an opposite phase, respectively. Furthermore, when the two driven emitters are axially symmetrical with respect to the auxiliary emitter, we have $\Omega_{13} = \Omega_{23}$ and $\gamma_{13} = \gamma_{23}$. Thus the opposite-phase photon exchange disappears due to the complete destructive interference, i.e., $\Omega_{-}^{(dd)} = \gamma_{-}^{(dd)} = 0$. Whereas the in-phase process couples the dressed states $|2\rangle$ with $|4\rangle$, and $|6\rangle$ with $|7\rangle$, through the effective coupling rates $\Omega_{+}^{(dd)} = \sqrt{2}A_1\Omega_r$ and $\gamma_{+}^{(dd)} = \frac{A_1}{\sqrt{2}}\gamma_r$ with $\Omega_r = \Omega_{13} = \Omega_{23}$ and $\gamma_r = \gamma_{13} = \gamma_{23}$. For clarity of analytical investigation but without losing generality, let us concentrate on this typical configuration, which contains all the physical mechanisms we are interested in. This isosceles triangle configuration can be structured by setting $\varphi_3 = \pi/2$ or $3\pi/2$.

A. Diagonalized atomic representation

Based on the spirit of filtering dynamics that the internal-state quantum dynamics of quantum radiating source is not affected by the presence of filters [61], we can first derive and solve the equations of motion for the degrees of freedom

of the three-body quantum antenna, i.e., the reduced density matrix elements of the source $\rho_{k'k} = \langle\sigma_{kk'}\rangle$, from the cascaded master equation given by Eqs. (8)–(11). In the considered isosceles triangle configuration, the atomic coherent effects caused by the dipole-dipole interaction between the dressed two-body radiating source and the auxiliary emitter give rise to the following steady-state density operator of the three-body quantum antenna in the dressed-state representation as

$$\rho_S = \sum_{k=1}^{8} \rho_{kk}|k\rangle\langle k| + (\rho_{24}|2\rangle\langle 4| + \rho_{42}|4\rangle\langle 2|),$$
$$+ (\rho_{67}|6\rangle\langle 7| + \rho_{76}|7\rangle\langle 6|), \quad (12)$$

where the nonzero steady-state density matrix elements ρ_{kk} ($k \in \{1, 2, \ldots, 8\}$), $\rho_{24}, \rho_{42}, \rho_{67}$, and ρ_{76} and their equations of motion have been given in Appendix B. As a set of states can always be found that transforms the steady-state density operator of the source into the incoherent superposition of several independent pure states, it seems convenient to introduce a new atomic basis $\{|\tilde{j}\rangle\}$ ($j \in \{1, 2, \ldots, 8\}$) by diagonalizing the steady-state density operator of the source ρ_S. In the new atomic basis, the uncorrelated atomic bases remain unchanged, i.e., $|\tilde{1}\rangle = |1\rangle$, $|\tilde{3}\rangle = |3\rangle$, $|\tilde{5}\rangle = |5\rangle$, and $|\tilde{8}\rangle = |8\rangle$, whereas two pairs of coherent superposition atomic states, $\{|\tilde{2}\rangle, |\tilde{4}\rangle\}$ and $\{|\tilde{6}\rangle, |\tilde{7}\rangle\}$, are introduced as

$$|\tilde{2}\rangle = \sin\alpha_1|2\rangle + \cos\alpha_1 e^{-i\phi_{24}}|4\rangle,$$
$$|\tilde{4}\rangle = -\cos\alpha_1 e^{i\phi_{24}}|2\rangle + \sin\alpha_1|4\rangle, \quad (13)$$

and

$$|\tilde{6}\rangle = \sin\alpha_2|6\rangle + \cos\alpha_2 e^{-i\phi_{67}}|7\rangle,$$
$$|\tilde{7}\rangle = -\cos\alpha_2 e^{i\phi_{67}}|6\rangle + \sin\alpha_2|7\rangle, \quad (14)$$

respectively, where the phase angles $\phi_{kk'}$ are determined by the atomic coherences $\rho_{kk'} = |\rho_{kk'}|e^{i\phi_{kk'}}$, and α_1 and α_2 are determined by the relations $\sin^2\alpha_1 = \frac{1}{2} + u_{24}/(2w_{24})$ and $\sin^2\alpha_2 = \frac{1}{2} + u_{67}/(2w_{67})$, respectively, with the definitions $u_{kk'} = \rho_{kk} - \rho_{k'k'}$ and $w_{kk'} = \sqrt{u_{kk'}^2 + 4|\rho_{kk'}|^2}$. Therefore the new representation transforms ρ_S into the diagonalized form

$$\tilde{\rho}_S = \sum_{j=1}^{8} \tilde{\rho}_{jj}|\tilde{j}\rangle\langle\tilde{j}|, \quad (15)$$

where the new steady-state populations $\tilde{\rho}_{22}, \tilde{\rho}_{44}, \tilde{\rho}_{66}$, and $\tilde{\rho}_{77}$ can be calculated straightforwardly from the original dressed-state populations and the atomic coherences via Eqs. (13) and (14).

B. Quantum state of the system in the diagonalized atomic representation

To calculate frequency-resolved correlation functions, the corresponding two-mode atom-photon correlators of the type $\langle a^{\dagger m}b^{\dagger p}b^q a^n \tilde{\sigma}_{rs}\rangle$ and the single-mode atom-photon correlators of the type $\langle a^{\dagger m}a^n \tilde{\sigma}_{rs}\rangle$ give us a good starting point, where $a, b \in \{a_1, a_2, a_3\}$ and $\tilde{\sigma}_{rs} = |\tilde{r}\rangle\langle\tilde{s}|$ is the transition operator between the two diagonalized atomic states $|\tilde{r}\rangle$ and $|\tilde{s}\rangle$. From the cascaded master equation (8)–(11), the equations of motion and the steady-state solutions for the correlators can be

derived, thus providing the exact description of the geometry-dependent spectrally correlations for the system. Here, it should be noted that the correlation properties of arbitrary two modes are unaltered by the presence of the residual mode due to the lack of its back action to the source, irrespective of its decay rate, and vice versa. Thus the correlators of the reduced system (source plus target modes) depending on which modes are chosen can be calculated by the corresponding reduced density operator after tracing out the remaining mode. In addition, the correlator $\langle a^{\dagger m} b^{\dagger p} b^q a^n \tilde{\sigma}_{rs} \rangle$ is of the order of $(\sqrt{\mu \kappa \gamma})^{m+p+q+n}$, which means that the dependence of the normalized correlations on the coupling rate $\sqrt{\mu \kappa \gamma}$ can vanish algebraically irrespective of the value of μ.

However, by recalling the spirit of quantum filtering dynamics that each filtered mode is produced under the weak-coupling regime between the source and filters with extremely weak excitation [61], we may consider that the weak-coupling regime allows the analytical expressions of the correlation functions to be accurately computed by truncating the Hilbert space. For two-mode correlations, the Hilbert space depending on which modes are chosen is spanned by a set of atom-photon collective bases $\{|\tilde{j}, n_a, n_b\rangle\}$, where the first index $\tilde{j}$ denotes the diagonalized atomic states, and the indexes n_a and n_b denote the excitations of the cavity modes a and b, respectively. Correspondingly, for single-mode dynamics, we introduce the atom-photon collective state vectors $\{|\tilde{j}, n_a\rangle\}$. Therefore the mth-order correlators with $m \in \{0, 1, 2\}$ can be calculated analytically by truncating the Hilbert space to one or two photons, i.e., we have $n_a, n_b \in \{0, 1\}$ for two-mode two-photon dynamics and $n_a \in \{0, 1, 2\}$ for single-mode two-photon dynamics.

As we expected, after ignoring higher-order coupling terms in the truncated density matrix elements due to the weak coupling, we can establish the one-to-one correspondence between the correlators and the approximate truncated density matrix elements. Despite the various mode combinations, we find that the approximate truncated reduced density operators of all the possible single-mode atom-photons combined systems $\tilde{\rho}_{S,a}$ and the two-mode atom-photons combined systems $\tilde{\rho}_{S,ab}$ can be summarized, respectively, as

$$\tilde{\rho}_{S,a} \approx \sum_{r,s} \sum_{m,n} \frac{\langle a^{\dagger m} a^n \tilde{\sigma}_{rs} \rangle}{\sqrt{m! n!}} |\tilde{s}, n_a\rangle \langle \tilde{r}, m_a|, \quad (16a)$$

$$\tilde{\rho}_{S,ab} \approx \sum_{r,s} \sum_{m,n} \sum_{p,q} \frac{\langle a^{\dagger m} b^{\dagger p} b^q a^n \tilde{\sigma}_{rs} \rangle}{\sqrt{m! n! p! q!}} |\tilde{s}, n_a.q_b\rangle \langle \tilde{r}, m_a, p_b|. \quad (16b)$$

We note here that, in Eq. (16b), the upper bounds of the summation indexes m_a, n_a, p_b, and q_b in the state vectors cannot be zero due to the fact that both modes have at least one photon in their respective cavities when we consider two-mode dynamics. Base on Eqs. (16a) and (16b), more transparent physical mechanisms can be revealed if the quantum antenna is resolved by the filter whose passband width κ is sufficiently larger than the spectral linewidth, i.e., $\kappa \gg \gamma$ [71,72]. Physically, on the one hand, the target cavity with large passband width can extract the entire target spectral component without spectral distortion. On the other hand, this situation ensures that the emissions triggered by each of the atomic states $|\tilde{j}\rangle$

can be individually addressable so that the total fluorescent emission can be treated as the incoherent superposition of independent emission groups [71,72], weighted by the new atomic populations $\tilde{\rho}_{jj}$, respectively. Therefore it may be beneficial to split the two-mode correlators according to the steady-state atomic populations $\tilde{\rho}_{jj}$ as the following form (see Appendix C):

$$\langle a^{\dagger m} b^{\dagger p} b^q a^n \tilde{\sigma}_{rs} \rangle = \sum_{j=1}^{8} \tilde{\rho}_{jj} \langle a^{\dagger m} b^{\dagger p} b^q a^n \tilde{\sigma}_{rs} \rangle_j. \quad (17)$$

As we expected, a more instructive relation is exposed now that all the reduced correlators $\langle a^{\dagger m} b^{\dagger p} b^q a^n \tilde{\sigma}_{rs} \rangle_j$ belonging to the common emission group triggered by the new atomic state $|\tilde{j}\rangle$ can be factorized as (see Appendix C)

$$\langle a^{\dagger m} b^{\dagger p} b^q a^n \tilde{\sigma}_{rs} \rangle_j = \langle a^{\dagger m} b^{\dagger p} \tilde{\sigma}_{rj} \rangle_j \langle a^n b^q \tilde{\sigma}_{js} \rangle_j. \quad (18)$$

This factorization relation implies a transparent case when $m = n$, $p = q$, and $r = s$ simultaneously. In this case, we find that the reduced correlator $\langle a^n b^q \tilde{\sigma}_{js} \rangle_j$ can serve as a probability amplitude through the relation $\langle (a^{\dagger} a)^n (b^{\dagger} b)^q \tilde{\sigma}_{ss} \rangle_j = |\langle a^n b^q \tilde{\sigma}_{js} \rangle_j|^2$, where $\langle (a^{\dagger} a)^n (b^{\dagger} b)^q \tilde{\sigma}_{ss} \rangle_j$ can be understood as the probability of detecting $(n + q)$ photons, including n photons in mode a and q photons in mode b, triggered from the atomic state $|\tilde{j}\rangle$ and terminated by the atomic state $|\tilde{s}\rangle$. The factorization for the single-mode correlators can be also found with similar form given by (C21) in Appendix C. Inspired by this decomposition, we find that the approximate truncated reduced density operators (16a) and (16b) can be simplified, respectively, as the following compact forms:

$$\tilde{\rho}_{S,a} = \sum_{j=1}^{8} \tilde{\rho}_{jj} |\tilde{\Psi}_{S,a}^{(j)}\rangle \langle \tilde{\Psi}_{S,a}^{(j)}|, \quad (19a)$$

$$\tilde{\rho}_{S,ab} = \sum_{j=1}^{8} \tilde{\rho}_{jj} |\tilde{\Psi}_{S,ab}^{(j)}\rangle \langle \tilde{\Psi}_{S,ab}^{(j)}|, \quad (19b)$$

where the steady-state single-mode wave functions and two-mode wave functions take the general forms

$$|\tilde{\Psi}_{S,a}^{(j)}\rangle = |\tilde{j}, 0_a\rangle + \sum_{(j', n_a)} \tilde{\mathcal{C}}_{j', n_a}^{(j)} |\tilde{j}', n_a\rangle, \quad (20a)$$

$$|\tilde{\Psi}_{S,ab}^{(j)}\rangle = |\tilde{j}, 0_a, 0_b\rangle + \sum_{(j', n_a, n_b)} \tilde{\mathcal{C}}_{j', n_a, n_b}^{(j)} |\tilde{j}', n_a, n_b\rangle, \quad (20b)$$

respectively. In Eqs. (20a) and (20b), the steady-state probability amplitude $\tilde{\mathcal{C}}_{j', n_a, n_b}^{(j)}$ $(\tilde{\mathcal{C}}_{j', n_a}^{(j)})$ describes all the possible cascaded emissions from the initial state $|\tilde{j}, 0_a, 0_b\rangle$ $(|\tilde{j}, 0_a\rangle)$ to the target state $|\tilde{j}', n_a, n_b\rangle$ $(|\tilde{j}', n_a\rangle)$, and the summation index (j', n_a, n_b) $[(j', n_a)]$ represents a possible state determined by the electric dipole transitions. The analytical expressions of the probability amplitudes are derived from the reduced correlators in the diagonalized atomic representation, and have been presented in Appendix D.

C. Quantum state of the system in the dressed-state representation

In order to explore the role of the atomic coherent effects established by the electric dipole-dipole interaction between the driven two-body radiating source and the

undriven auxiliary emitter, we now transform $\tilde{\rho}_{S,ab}$ back to the original dressed-state representation via the transformations (13) and (14). Thus we regain the steady-state density operator of the full system, including the source in the dressed-state representation and the target cavity modes, as

$$\rho_{S,a} = \sum_{k=1}^{8} \rho_{kk} |\Psi_{S,a}^{(k)}\rangle\langle\Psi_{S,a}^{(k)}| + \left(\rho_{24}|\Psi_{S,a}^{(2)}\rangle\langle\Psi_{S,a}^{(4)}| + \text{H.c.}\right) + \left(\rho_{67}|\Psi_{S,a}^{(6)}\rangle\langle\Psi_{S,a}^{(7)}| + \text{H.c.}\right), \tag{21a}$$

$$\rho_{S,ab} = \sum_{k=1}^{8} \rho_{kk} |\Psi_{S,ab}^{(k)}\rangle\langle\Psi_{S,ab}^{(k)}| + \left(\rho_{24}|\Psi_{S,ab}^{(2)}\rangle\langle\Psi_{S,ab}^{(4)}| + \text{H.c.}\right) + \left(\rho_{67}|\Psi_{S,ab}^{(6)}\rangle\langle\Psi_{S,ab}^{(7)}| + \text{H.c.}\right), \tag{21b}$$

where the explicit forms of the steady-state single-mode wave functions $|\Psi_{S,a}^{(k)}\rangle$ and the two-mode wave functions $|\Psi_{S,ab}^{(k)}\rangle$ are similar to $|\tilde{\Psi}_{S,a}^{(j)}\rangle$ in Eq. (20a) and $|\tilde{\Psi}_{S,ab}^{(j)}\rangle$ in Eq. (20b), respectively, and are given by

$$\left|\Psi_{S,a}^{(k)}\right\rangle = |k, 0_a\rangle + \sum_{(k',n_a)} \mathcal{C}_{k',n_a}^{(k)}|k', n_a\rangle, \tag{22a}$$

$$\left|\Psi_{S,ab}^{(k)}\right\rangle = |k, 0_a, 0_b\rangle + \sum_{(k',n_a,n_b)} \mathcal{C}_{k',n_a,n_b}^{(k)}|k', n_a, n_b\rangle. \tag{22b}$$

In Eqs. (22a) and (22b), the cascaded transitions described by $\mathcal{C}_{k',n_a,n_b}^{(k)}$ ($\mathcal{C}_{k',n_a}^{(k)}$) are similar to those described by the probability amplitude $\tilde{\mathcal{C}}_{j',n_a,n_b}^{(j)}$ ($\tilde{\mathcal{C}}_{j',n_a}^{(j)}$) so that $\mathcal{C}_{k',n_a,n_b}^{(k)}$ ($\mathcal{C}_{k',n_a}^{(k)}$) and $\tilde{\mathcal{C}}_{j',n_a,n_b}^{(j)}$ ($\tilde{\mathcal{C}}_{j',n_a}^{(j)}$) share the common analytical forms, which has been presented in Appendix D. In physical terms, the first term of Eqs. (21a) and (21b) represents the incoherent superposition of different cascaded emission groups weighted by the populations ρ_{kk}, respectively, while the second and the third terms of Eqs. (21a) and (21b) illustrate the interferences of the cascaded emission groups triggered by the correlated atomic states $\{|2\rangle, |4\rangle\}$ and $\{|6\rangle, |7\rangle\}$, respectively.

In Fig. 2, the steady-state atomic populations and the atomic coherences of the quantum antenna for the isosceles triangle configuration are plotted for the parameters $r_{12} = r_3 = 0.2\lambda_0$, $\Omega = 100\gamma$, and $\theta_d = 0$. It is clearly seen that the maximal magnitude of the atomic coherence ρ_{24} is almost twice that of ρ_{67}, which is more important for the regulation of directional emissions than the latter. The dominant coherence ρ_{24} arises from the large population of the dressed state $|2\rangle$ prepared by the laser field with negative detuning, $\Delta < 0$. Whereas the maximal values of ρ_{66} and ρ_{77} in Fig. 2(b) are 0.225 and 0.042, respectively, which are far less than the value of ρ_{22} in the region of $\Delta < 0$. This unbalanced distribution of the atomic populations and coherences can be illustrated by the explicit forms of the dressed states $|2\rangle = |+_1, +_2, g_3\rangle$ and $|4\rangle = \frac{1}{\sqrt{2}}(|+_1, -_2, e_3\rangle + |-_1, +_2, e_3\rangle)$, in which $|+_i\rangle = c|e_i\rangle + s|g_i\rangle$ and $|-_i\rangle = -s|e_i\rangle + c|g_i\rangle$ ($i = 1, 2$) are the single-atom dressed states. One can see that, for $\Delta < 0$, the probability of the two dressed quantum emitters being prepared in the single-atom dressed state $|+\rangle$ simultaneously can be enhanced significantly, such as $\rho_{22} = 0.94$ for $\Delta = -100\gamma$. This leads to the enhancement of the emission of the higher-frequency sideband photons and the resonant dipole-dipole interaction

between the two-body dressed radiating source and the undriven emitter. Whereas the population of the state $|8\rangle = |-_1, -_2, g_3\rangle$, which is related to the emission of the lower-frequency sideband photons, is suppressed for large negative laser detunings, as illustrated by the black dashed line in Fig. 2(a). It should be noted that the coherence ρ_{24} can be subverted by very large laser detunings. Thus the value of Δ should be chosen approvingly to ensure a sufficient atomic population ρ_{22} and the sensitive dependence of the photon correlation signals on the atomic coherence ρ_{24}.

Now we would like to discuss the obtained analytical forms briefly. Firstly, one can see that the state of the system, $\rho_{S,ab}$, is classified by the incoherent superposition part and the interference part, where the incoherent superposition part are further classified according to different dressed-state radiating sources (ρ_{kk}). Therefore their respective contributions to the total correlation signals are transparent analytically. Secondly, it is straightforward to recover the analytical results for a strongly dressed two-atom system by setting the distance r_3 to infinity. To our knowledge, the directionality of spectral correlations in this system with electric dipole-dipole inter-
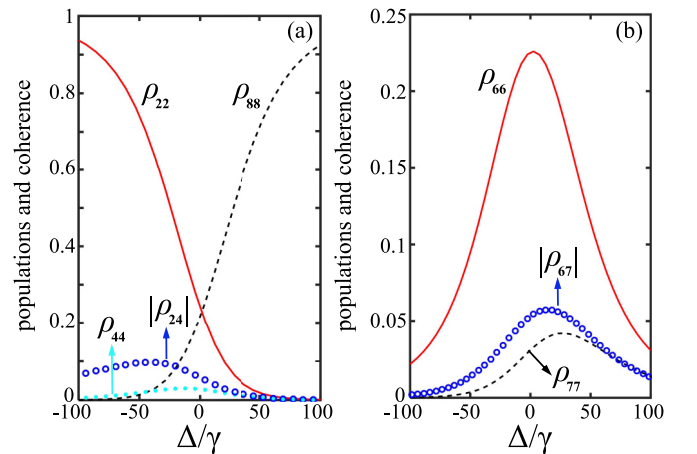

FIG. 2. Steady-state populations and atomic coherences of the three-body dressed states for the isosceles triangle configuration, plotted as functions of the laser detuning Δ. (a) ρ_{22} (red solid line), ρ_{88} (black dashed line), ρ_{44} (cyan dotted line), and $|\rho_{24}|$ (blue circular line). (b) ρ_{66} (red solid line), ρ_{77} (black dashed line), and $|\rho_{67}|$ (blue circular line). The parameters are $r_{12} = r_3 = 0.2\lambda_0$, $\Omega = 100\gamma$, and $\theta_d = 0$.

action being considered have not been studied so far. We hope that our investigation for the three-body quantum antenna can provide some complementary results for this system, which will be discussed later. In addition, we can also check that the nth-order spectral correlation signals (such as intensity or intensity correlation) calculated from our analytical approach can be reproduced via the conventional physical spectrum with $2n$-time integrals [71,72].

IV. DIRECTIONAL NONCLASSICALITY OF FREQUENCY-RESOLVED SPECTRAL CORRELATIONS

Before exploring the geometry-dependent nonclassical correlations generated from the three-body quantum antenna, let us first consider the experimental feasibility of the parameters of the quantum filtering dynamics in our scheme. The experimental researches for the frequency-resolved spectral correlations of the Mollow photons were carried out in single semiconductor quantum dots, as presented in Ref. [40]. The experimental parameters in Ref. [40] are under the regime of large filter bandwidth, corresponding to the condition considered in Refs. [71,72], in which the filter bandwidth κ and the radiative natural linewidth of the quantum dot γ satisfy $\kappa = 12\gamma$ for $\kappa^{-1} = 110$ ps and $\gamma^{-1} = 1.25(+0.08)$ ns. Recently, the photon statistics of filtered resonance fluorescence was also reported in Ref. [44], in which the fluorescent photons generated from a self-assembled quantum dot are filtered by a Lorentzian filter with the tunable linewidth from narrow ($\kappa = 0.01\gamma$) to wide ($\kappa = 100\gamma$). Based on these experimental conditions, we choose the large filter linewidth $\kappa = 20\gamma$ considered in Refs. [71,72], which has been achieved experimentally. In addition, the scattered fluorescent photons are expected to be collected efficiently in experimental schemes [42,43]. Thus, for the cascaded driving scheme in our system, a properly large fraction of fluorescent emission of single emitter reaching the filter may be more in line with experimental demands, although the normalized correlation functions are independent of the value of μ. Base on this consideration, we choose $\mu = 0.8$ as discussed in Refs. [63,64,73] for the calculations of unnormalized correlation functions, which covers the emitted photons at a large solid angle of single-emitter spontaneous emission. In particular, within the framework of chiral quantum optics, optical nanofibres and waveguides can provide the possibility of fully unidirectional spontaneous emission to realize cascaded quantum systems, even for insignificant unidirectional modes [14].

A. Geometry-dependent nonclassicality related to intensity-intensity correlations

An elegant way to test the nonclassical correlations between two quantized modes a and b is the Cauchy-Schwarz inequality. The version of intensity-intensity correlation functions can be expressed as [41,42,74]

$$\mathcal{R}_{ab}^{(2)} = \frac{\left(G_{ab}^{(2)}\right)^2}{G_a^{(2)} G_b^{(2)}} \leqslant 1, \tag{23}$$

where $G_{ab}^{(2)} = \langle a^\dagger b^\dagger b a \rangle$ is the intensity-intensity correlation between modes a and b, $G_a^{(2)} = \langle a^{\dagger 2} a^2 \rangle$ and $G_b^{(2)} = \langle b^{\dagger 2} b^2 \rangle$

are the single-mode intensity-intensity correlations of modes a and b, respectively. The parameter $\mathcal{R}_{ab}^{(2)}$ is defined to quantify the degree of the violation of the Cauchy-Schwarz inequality, and two-mode nonclassical correlations are indicated by $\mathcal{R}_{ab}^{(2)} > 1$.

We first plot in Figs. 3(a)–3(d) the violation degrees of the Cauchy-Schwarz inequality $\mathcal{R}_{a_1 a_2}^{(2)}$ and the relevant intensity-intensity correlations in the xy plane varying with the single observation angle $\phi_l = \phi$ for the small distance $r_{12} = 0.3\lambda_0$ in Figs. 3(a) and 3(b), and for the larger distance $r_{12} = 1.5\lambda_0$ in Figs. 3(c) and 3(d). Other parameters are $\Omega = -\Delta = 100\gamma$, $r_3 = 0.2\lambda_0, \kappa = 20\gamma, \delta_1 = \bar{\Omega}$, and $\delta_2 = 0$. The undriven emitter is placed at the xy plane, i.e., $\vartheta_3 = \pi/2$, and the dipole orientations are assumed to be perpendicular to the observation plane, i.e., $\theta_d = 0$. Figs. 3(a) and 3(c) show that the violation degrees of the Cauchy-Schwarz inequality of the photon pair (a_1, a_2), i.e., $\mathcal{R}_{a_1 a_2}^{(2)}$, display obvious rotational symmetry despite the presence of the auxiliary emitter. Under the same parameters, by comparing the intensity-intensity correlations in Figs. 3(b) and 3(d) with the degrees of the violation of the Cauchy-Schwarz inequality $\mathcal{R}_{a_1 a_2}^{(2)}$ in Figs. 3(a) and 3(c), respectively, one can observe that the maximal two-photon probabilities of the single-mode field a_2 (blue curves in Figs. 3(b) and 3(d) corresponding to $G_{a_2}^{(2)} \times 10^3$) are almost one order of magnitude higher than the probabilities of the two-mode photon pair $G_{a_1 a_2}^{(2)}$ [red curves in Figs. 3(b) and 3(d) corresponding to $G_{a_1 a_2}^{(2)} \times 10^4$] and the single-mode photon pair $G_{a_1}^{(2)}$ (green curves in Figs. 3(b) and 3(d) corresponding to $G_{a_1}^{(2)} \times 10^4$). These results originate from the fact that it is the central-peak photon pair that is resonant with two dressing photons. Therefore only the concave parts of the angular distributions of $G_{a_2}^{(2)}$ lead to the nonclassical lobes of $\mathcal{R}_{a_1 a_2}^{(2)}$.

However, the situation for the two opposite sideband photons, i.e., the photon pair (a_1, a_3), is radically different. As presented in Fig. 3(e), the giant but rotationally asymmetrical nonclassicality displays in the direction $\phi = \pi/2$ under the same parameters as in Figs. 3(a) and 3(b) except for $\delta_3 = -\bar{\Omega}$. Furthermore, the larger distance $r_{12} = \lambda_0$ in Fig. 3(g) not only increases the number of nonclassical lobes of $\mathcal{R}_{a_1 a_3}^{(2)}$, but also makes the maximal nonclassicality more concentrated. After examining the corresponding two-photon joint probabilities in Figs. 3(f) and 3(h), corresponding to Figs. 3(e) and 3(g), respectively, we find that the directionality of $\mathcal{R}_{a_1 a_3}^{(2)}$ is dominated by $G_{a_1 a_3}^{(2)}$ [blue curves in Figs. 3(f) and 3(h)], instead of the single-mode two-photon emissions as in the previous group.

Now let us explore the physical mechanisms of the directionally nonclassical correlations of the two-mode photon pair (a_1, a_3). Given the analytical approach proposed in Sec. III, the full intensity-intensity correlation function $G_{a_1 a_3}^{(2)}$ is calculated, which is given by Eqs. (E1) and (E2) in Appendix E. The full solution of $G_{a_1 a_3}^{(2)}$ includes the contributions of all the atomic populations ($\rho_{11}, \rho_{22}, \ldots, \rho_{88}$) and atomic coherences ($\rho_{24}, \rho_{42}, \rho_{67}, \rho_{76}$). However, in order to enhance the higher-frequency collective emissions, the three-body quantum antenna is mainly populated to the dressed state $|2\rangle$ for an appropriate negative laser detuning. This leads the cascaded emissions of the two-mode sideband fields (a_1, a_3) to be concentrated on a pair of correlated cascaded emission groups,
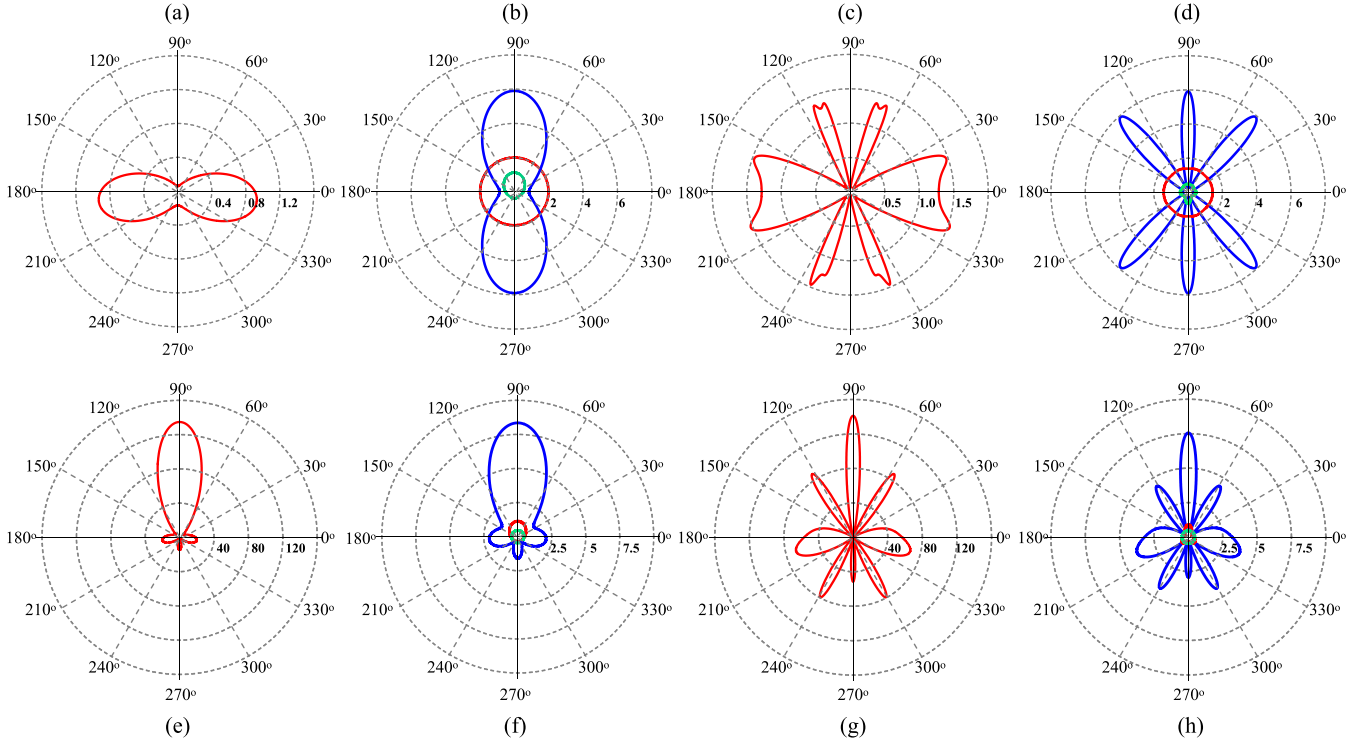
FIG. 3. Polar diagrams of the violation degrees of the Cauchy-Schwarz inequality $\mathcal{R}^{(2)}_{a_1a_2}$, $\mathcal{R}^{(2)}_{a_1a_3}$, and the relevant two-photon correlations as functions of the single-observation angle $\phi_l = \phi$ with $\theta_d = 0$. For the photon pair (a_1, a_2): (a) and (c) $\mathcal{R}^{(2)}_{a_1a_2}$, (b) and (d) $G^{(2)}_{a_1a_2} \times 10^4$ (red curves), $G^{(2)}_{a_1} \times 10^4$ (green curves), and $G^{(2)}_{a_2} \times 10^3$ (blue curves), in which (b) corresponds to (a) for $r_{12} = 0.3\lambda_0$, and (d) corresponds to (c) for $r_{12} = 1.5\lambda_0$. For the photon pair (a_1, a_3): (e) and (g) $\mathcal{R}^{(2)}_{a_1a_3}$, (f) and (h) $G^{(2)}_{a_1a_3} \times 10^4$ (blue curves), $G^{(2)}_{a_1} \times 10^4$ (red curves), and $G^{(2)}_{a_3} \times 10^4$ (green curves), in which (f) corresponds to (e) for $r_{12} = 0.3\lambda_0$, and (h) corresponds to (g) for $r_{12} = \lambda_0$. Other parameters are $\Omega = -\Delta = 100\gamma$, $\kappa = 20\gamma$, $\mu = 0.8$, $\theta_l = \pi/2$, $r_3 = 0.2\lambda_0$, $\vartheta_3 = \pi/2$, $\delta_1 = \bar{\Omega}$, $\delta_2 = 0$, and $\delta_3 = -\bar{\Omega}$.

triggered by the dressed states $|2\rangle$ and $|4\rangle$. Thus the dominant two-photon correlation signal $G^{(2)}_{a_1a_3}$ is the consequence of probing the common two-photon state $|2, 1_{a_1}, 1_{a_3}\rangle$ of this pair of correlated cascaded emission groups, as illustrated in Fig. 4. The value of $G^{(2)}_{a_1a_3}$ is predominately contributed from the four-channel interference in this pair of cascaded emission
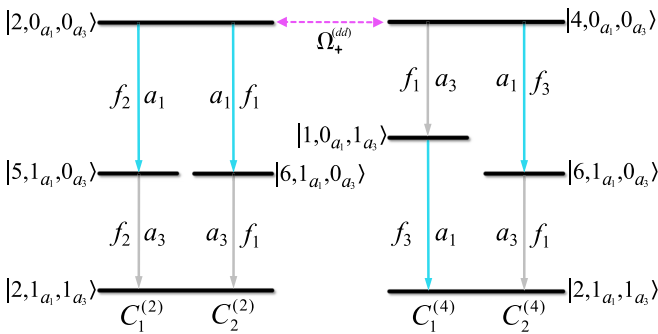

FIG. 4. Dominant two-photon cascaded emissions of the two-mode fields (a_1, a_3) described by $\tilde{G}^{(2)}_{a_1a_3}$. The interfered cascaded emission groups are triggered by the initial dressed states $|2\rangle$ and $|4\rangle$, respectively, and terminated by their common two-photon target state $|2, 1_{a_1}, 1_{a_3}\rangle$. The fluorescent photons generated from the higher-frequency component (blue arrows) and the lower-frequency component (gray arrows) are coupled by the cavity modes a_1 and a_3, respectively. The geometry factors of single-photon transitions are indicated.

groups, and their corresponding two-photon probability amplitudes are labeled as $\mathcal{C}^{(2)}_1$, $\mathcal{C}^{(2)}_2$, $\mathcal{C}^{(4)}_1$, and $\mathcal{C}^{(4)}_2$, respectively, as indicated in Fig. 4. Obviously, our target two-photon probability amplitudes are $\mathcal{C}^{(2)}_{2,1_{a_1},1_{a_3}} = \mathcal{C}^{(2)}_1 + \mathcal{C}^{(2)}_2$ and $\mathcal{C}^{(4)}_{2,1_{a_1},1_{a_3}} = \mathcal{C}^{(4)}_1 + \mathcal{C}^{(4)}_2$. For convenience, let we introduce an abbreviation "$\tilde{G}^{(n)}_{ab}$" to represent the main contribution of the value of total nth-order correlation function $G^{(n)}_{ab}$. Thus the contribution of the four-channel interference can be calculated as

$$\tilde{G}^{(2)}_{a_1a_3} = \sum_{k=2,4} \mathcal{P}^{(kk)} + \sum_{j,j'=1,2} \mathcal{P}^{(24)}_{jj'}, \tag{24}$$

where the probability components are

$$\mathcal{P}^{(22)} = \rho_{22}\left|\mathcal{C}^{(2)}_{2,1_{a_1},1_{a_3}}\right|^2, \quad \mathcal{P}^{(44)} = \rho_{44}\left|\mathcal{C}^{(4)}_{2,1_{a_1},1_{a_3}}\right|^2,$$

$$\mathcal{P}^{(24)}_{jj'} = 2\text{Re}\left[\rho_{42}\left(\mathcal{C}^{(2)*}_j \mathcal{C}^{(4)}_{j'}\right)\right] \quad (j, j' = 1, 2). \tag{25}$$

The values of the dominant contribution $\tilde{G}^{(2)}_{a_1a_3}$ and the total correlation function $G^{(2)}_{a_1a_3}$ are compared in Fig. 5(a) to verify the accuracy of the analytical results. In Eq. (25), the function $\mathcal{P}^{(kk)}$ represents the two-photon joint probability of a pair of channels belonging to a common cascaded emission group, and $\mathcal{P}^{(24)}_{jj'}$ represents the interference between the two channels belonging to different cascaded emission groups. Their analytical expressions are further derived with the help of the analytical forms in Eqs. (21b) and (22b), and are given by

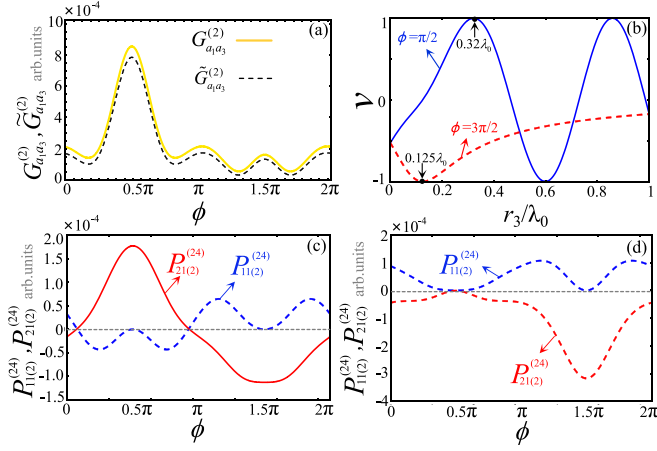$$\mathcal{P}^{(22)} = \xi^4 A_1^2 A_2^2 \rho_{22}\mathcal{E}^{(22)},$$

FIG. 5. (a) Comparison of the angular distributions of the total two-photon correlation $G^{(2)}_{a_1a_3}$ (yellow solid line) calculated by Eq. (E1) and the contribution of the interfered four channels $\tilde{G}^{(2)}_{a_1a_3}$ (black dashed line) given by Eq. (24). (b) Geometrical modulation function $v(r_3, \phi) = \cos \psi_3$ varying with the distance r_3 for $\phi = \pi/2$ (blue solid line) and $\phi = 3\pi/2$ (red dashed line) with $r_{12} = 0.3\lambda_0$. (c) and (d) Angular distributions of the interference terms $\mathcal{P}^{(24)}_{11}$ ($= \mathcal{P}^{(24)}_{12}$) (blue dashed lines) and $\mathcal{P}^{(24)}_{21}$ ($= \mathcal{P}^{(24)}_{22}$) (red solid lines) for (c) $r_3 = 0.32\lambda_0$ and (d) $r_3 = 0.125\lambda_0$ determined from (b). All the other parameters in (a)−(d) are the same as in Figs. 3(e) and 3(f).

$$\mathcal{P}^{(44)} = 8\xi^4 A_2^2 \rho_{44} \mathcal{E}^{(44)},$$

$$\mathcal{P}^{(24)}_{11} = \mathcal{P}^{(24)}_{12} = \sqrt{2}\xi^4 A_1 A_2^2 |\rho_{24}| \mathcal{E}^{(24)}_1,$$

$$\mathcal{P}^{(24)}_{21} = \mathcal{P}^{(24)}_{22} = \sqrt{2}\xi^4 A_1 A_2^2 |\rho_{24}| \mathcal{E}^{(24)}_2, \quad (26)$$

where $\xi = \sqrt{\mu\kappa\gamma}/\kappa$. The geometrical modulation functions in Eq. (26) are given by

$$\mathcal{E}^{(22)} = 16 \cos^2(2\psi_{12}),$$

$$\mathcal{E}^{(44)} = 4 \cos^2 \psi_{12},$$

$$\mathcal{E}^{(24)}_1 = [4\cos(3\psi_{12}) - 4\cos\psi_{12}] \cos \psi_3,$$

$$\mathcal{E}^{(24)}_2 = [4\cos(3\psi_{12}) + 12\cos\psi_{12}] \cos \psi_3, \quad (27)$$

where $\psi_{12} = \frac{1}{2}k_0 r_{12} \cos \phi$ and $\psi_3 = k_0 r_3 \sin \phi - \phi_{24}$. Eqs. (26) and (27) show that the angular distributions of $\mathcal{P}^{(22)}$ and $\mathcal{P}^{(44)}$ are rotationally symmetrical, i.e., we have the relations $\mathcal{P}^{(kk)}(\phi) = \mathcal{P}^{(kk)}(\pi \pm \phi)$ ($k \in 2, 4$). The symmetry of $\mathcal{P}^{(22)}$ can be traced back to the symmetrical geometrical structure of the driven two-emitter subsystem, whereas the symmetry of $\mathcal{P}^{(44)}$ is originated from the fact that the three-body cooperative mode a_1 is involved in the two possible two-photon cascaded transitions with opposite emission orderings, i.e., $|4\rangle \xrightarrow{a_3} |1\rangle \xrightarrow{a_1} |2\rangle$ and $|4\rangle \xrightarrow{a_1} |6\rangle \xrightarrow{a_3} |2\rangle$, as illustrated in Fig. 4. However, for zero-delay detection, these two possible emission orderings are equivalent physically. Thus these two components convey the information about the emission orderings instead of the information about the photon exchanges, which is necessary for the directionality of emissions. Under such circumstances, the rotational asymmetry of the two-mode nonclassical correlations should be attributed to the second

term of Eq. (24), where the directional regulation relies more sensitively on $\mathcal{P}^{(24)}_{21}$ and $\mathcal{P}^{(24)}_{22}$ because the two-body symmetrically superposed mode (f_1) leads to a larger range of variation of the signal. Considering that the strong directionality refers to the ability of quantum antenna to produce prominent signal in special directions, it is possible to achieve the most significant nonclassical signal when the interference terms $\mathcal{P}^{(24)}_{21}$ and $\mathcal{P}^{(24)}_{22}$ are maximal. According to Eq. (27), the most satisfactory condition of maximal constructive interference is given by

$$\cos(3\psi_{12}) = \cos \psi_{12} = \cos \psi_3 = 1. \quad (28)$$

Here one might argue that the observation angles solved from the condition $\cos(3\psi_{12}) = \cos \psi_{12} = 1$ may not necessarily maximize the term $\cos \psi_3$ to $\cos \psi_3 = 1$. However, the analytical results in Eq. (27) tell us that the geometrical modulation effects of the driven two-emitter subsystem and the undriven emitter are completely separated, thus the undriven emitter can be controlled individually. Our strategy is to find the solutions of $\cos(3\psi_{12}) = \cos \psi_{12} = 1$, and then control the value of the geometrical modulation function $v(r_3, \phi) = \cos \psi_3$ conditioned by the solved angles.

We first examine the geometrical modulation effect of the driven two-emitter subsystem, i.e., the condition $\cos(3\psi_{12}) = \cos \psi_{12} = 1$. One can notice that $\cos \psi_{12} = 1$ is a sufficient but not necessary condition for $\cos(3\psi_{12}) = 1$. Thus the maximal constructive interference should be subject to the condition $\cos \psi_{12} = 1$, i.e.,

$$k_0 r_{12} \cos \phi = 4n\pi, \quad n \in \{0, \pm1, \pm2, \dots\}, \quad (29)$$

with the restriction on the distance of $r_{12} \geqslant |2n|\lambda_0 \geqslant 0$. This condition implies that the optimal enhancement of the terms $\cos(3\psi_{12})$ and $\cos \psi_{12}$ can be achieved for arbitrary value of r_{12}. Obviously, only the directions $\phi = \pi/2$ and $3\pi/2$ are available for a shorter distance r_{12}, which can inhibit the emergence of other lobes to generate unidirectional nonclassical correlation along the central vertical line of the driven two-emitter subsystem. In these two directions, it can be checked that the other two interference terms $\mathcal{P}^{(24)}_{11} = \mathcal{P}^{(24)}_{12} = 0$. Figure 5(b) shows the geometrical modulation function $v(r_3, \phi) = \cos \psi_3$ conditioned by the solved angles $\phi = \pi/2$ (blue solid line) and $\phi = 3\pi/2$ (red dashed line) for $r_{12} = 0.3\lambda_0$. We can determine that $r_3 \approx 0.32\lambda_0$ is the required distance in the range of $r_3 < \lambda_0/2$, corresponding to the maximal constructive interference and giving rise to the maximal nonclassical signal for the sideband photon pair (a_1, a_3). It is also worthwhile pointing out that another distance $r_3 \approx 0.125\lambda_0$ may suppress the value of $G^{(2)}_{a_1a_3}$ at $\phi = 3\pi/2$ optimally to realize the unidirectional two-mode nonclassicality in the direction $\phi = \pi/2$. In Figs. 5(c) and 5(d), the angular distributions of the interference terms illustrate the above discussions. Obviously, the inter-group interference is mainly dominated by $\mathcal{P}^{(24)}_{21}$ and $\mathcal{P}^{(24)}_{22}$, in which the maximal constructive interference occurs in the direction $\phi = \pi/2$ for $r_3 = 0.32\lambda_0$ [see red solid line in Fig. 5(c)], and the optimal destructive interference occurs in the direction $\phi = 3\pi/2$ for $r_3 = 0.125\lambda_0$ [see red solid line in Fig. 5(d)]. As for the appearance of the other lobes shown in Figs. 3(g) and 3(h) for the lager distance $r_{12} = \lambda_0$, it is predicted by the dominated symmetrical contribution $\mathcal{P}^{(22)}_{21}$, i.e., the condition of $\cos^2(2\psi_{12}) = 1$, yielding the directions

$\phi = 0$, $\pi/3$, $\pi/2$, $2\pi/3$, π, $4\pi/3$, and $5\pi/3$. However, the rotational asymmetry is still related to the inter-group interference due to the presence of the auxiliary undriven emitter.

B. Geometry-dependent nonclassicality related to intensity-field correlation

For the frequency-resolved two-mode correlations between the higher-frequency component and the central-frequency component, we have seen that the directionality of the violation of the Cauchy-Schwarz inequality related to intensity-intensity correlations displays obvious rotational symmetry. However, the next version can be considered to be customized for the special directionality of the nonclassical correlations between the modes a_1 and a_2.

As the concept of quantum correlations develops more and more extensively, the Cauchy-Schwarz inequality can be also specified by the so-called intensity-field correlation or wave-particle correlation [45–51], which has been attracting wide attention in recent years. The Cauchy-Schwarz inequality of this alternative version takes the form

$$\langle a^{\dagger 2} a^2 \rangle \langle :b_x^2: \rangle \geqslant \langle :a^\dagger b_x a: \rangle^2, \tag{30}$$

where the symbol "$\langle : : \rangle$" stands for the normally ordered expectation value of the operators of quantized fields, and $b_x = b e^{-ix} + b^\dagger e^{ix}$ is the quadrature amplitude of the mode b with x being the local oscillator phase in homodyne detection. This version can be obtained from the general Cauchy-Schwarz inequality $\langle :f_1^\dagger f_1: \rangle \langle :f_2^\dagger f_2: \rangle \geqslant |\langle :f_1^\dagger f_2: \rangle|^2$ by choosing $f_1 = a^\dagger a$ and $f_2 = b_x$ [47,75]. Since the two operators $a^\dagger a$ and b_x are Hermitian, the intensity-field correlation $\langle :a^\dagger b_x a: \rangle$ can be measured experimentally by conditional homodyne detection [50,51]. In the following, we shall label the intensity-field correlation and the quadrature squared as $G_{ab}^{(1.5)} = \langle :a^\dagger b_x a: \rangle$ and $X_b^{(1)} = \langle :b_x^2: \rangle$, respectively, where the superscript "(1.5)" represents that intensity-field correlation refers to "(intensity)$^{1.5}$". Here we should notice an important difference between Eqs. (30) and (23) that the quadrature squared signal can be negative, marking the absolute nonclassicality. Therefore a straightforward indicator for testing nonclassical correlations can be defined as

$$\mathcal{D}_{ab}^{(1.5)} = \left(G_{ab}^{(1.5)} \right)^2 - G_a^{(2)} X_b^{(1)}, \tag{31}$$

regardless of the sign of $X_b^{(1)}$, and $\mathcal{D}_{ab}^{(1.5)} > 0$ indicates nonclassical correlations. Meanwhile, an alternative violation degree is also available if $X_b^{(1)}$ is nonzero, which is defined as

$$\mathcal{R}_{ab}^{(1.5)} = \frac{\left(G_{ab}^{(1.5)} \right)^2}{G_a^{(2)} X_b^{(1)}}. \tag{32}$$

Thus the nonclassical correlations of radiation can be determined by $\mathcal{R}_{ab}^{(1.5)} > 1$ for $X_b^{(1)} > 0$ and $\mathcal{R}_{ab}^{(1.5)} < 1$ for $X_b^{(1)} < 0$. The signal $G_{ab}^{(n)}$ in our quantum filtering system is the $2n$th-order small quantity of the weak coupling rate $\sqrt{\mu\kappa\gamma}$, i.e., $G_{ab}^{(n)} \sim (\sqrt{\mu\kappa\gamma})^{2n}$. Therefore, compared with $\mathcal{D}_{ab}^{(1.5)}$, the function $\mathcal{R}_{ab}^{(1.5)}$ may be more sensitive to two-photon correlations and quadrature squared signals, thus can produce more prominent values for testing the nonclassical correlations in our quantum filtering system.
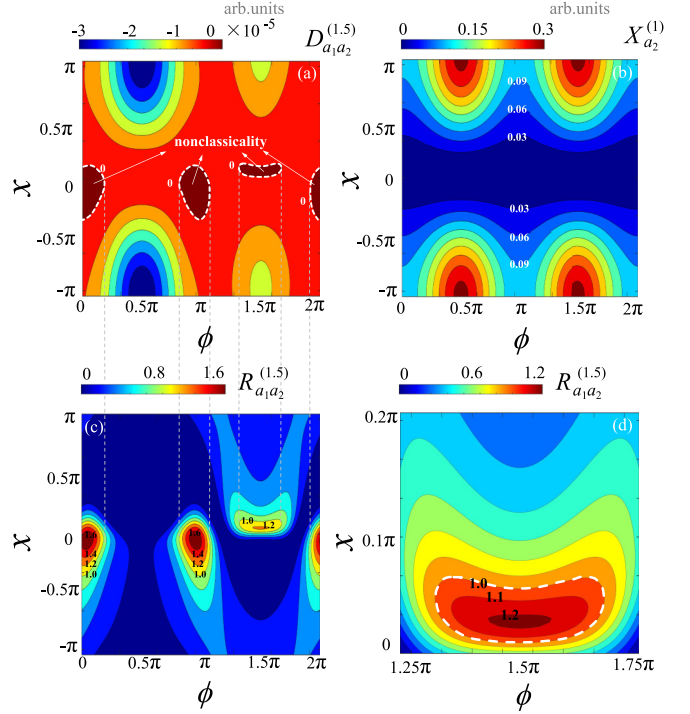

FIG. 6. The violation degrees of the Cauchy-Schwarz inequality (a) $\mathcal{D}_{a_1 a_2}^{(1.5)}$, (c) $\mathcal{R}_{a_1 a_2}^{(1.5)}$, and (b) the quadrature squared $X_{a_2}^{(1)}$ as a function of the single observation angle $\phi_l = \phi$ and the local oscillator phase x. Other parameters are $r_{12} = r_3 = 0.3\lambda_0$, $\Omega = -\Delta = 100\gamma$, $\kappa = 20\gamma$, $\mu = 0.8$, $\theta_l = \pi/2$, $\theta_d = 0$, $\vartheta_3 = \pi/2$, $\delta_1 = \bar{\Omega}$, and $\delta_2 = 0$. (d) Enlarged view of the distribution of the violation degree of the Cauchy-Schwarz inequality $\mathcal{R}_{a_1 a_2}^{(1.5)}$ around the direction $\phi = 3\pi/2$ in (c). In (a)−(d), the contours indicating the regions of nonclassicality are indicated by the white dashed thick curves, and the consistency of the regions of nonclassicality in (a) and (c) are indicated by the vertical dashed thin lines.

In our system, one of the intensity-field correlator in $G_{ab}^{(1.5)}$ is calculated as $\langle a^\dagger b a \rangle = \sum_k \langle k, 1_a, 1_b | \rho_{S,ab} | k, 1_a, 0_b \rangle$, i.e., we have the relation $\langle k, 1_a, 0_b | a^\dagger b a | k', 1_a, 1_b \rangle = \delta_{kk'}$ with $\delta_{kk'}$ being the Kronecker symbol. It means that the intensity-field correlator in our system extracts the information of the second-step transitions between the single-photon state and the two-photon state with unchanged atomic state. Obviously, only the photons emitted from the central-frequency component satisfy this requirement, and $\langle a_1^\dagger a_1 a_3 \rangle \equiv 0$ in our system.

In Fig. 6(a), we first explore the function $\mathcal{D}_{a_1 a_2}^{(1.5)}$ varying with the single-point observation angle $\phi_l = \phi$ and the local oscillator phase x. Under the given parameters, it can be observed that the nonclassical signals can emerge when the local oscillator phase is adjusted to $x \approx 0$. The reason can be explained by Fig. 6(b) that the optimal local oscillator phase in Fig. 6(a) corresponds to the reduction of the quadrature squared signal. Considering that the value of $X_{a_2}^{(1)}$ is positive in the whole region in Fig. 6(b), we further present the function $\mathcal{R}_{a_1 a_2}^{(1.5)}$ in Fig. 6(c) to visualize the nonclassical regions more clearly, in which the three distinct nonclassical peaks can be observed near the directions $\phi = 0$ (2π), $\phi = \pi$, and $\phi = 3\pi/2$, respectively. Obviously, the emergence of the nonclassicality around the direction $\phi = 3\pi/2$ [see Fig. 6(d)] realizes
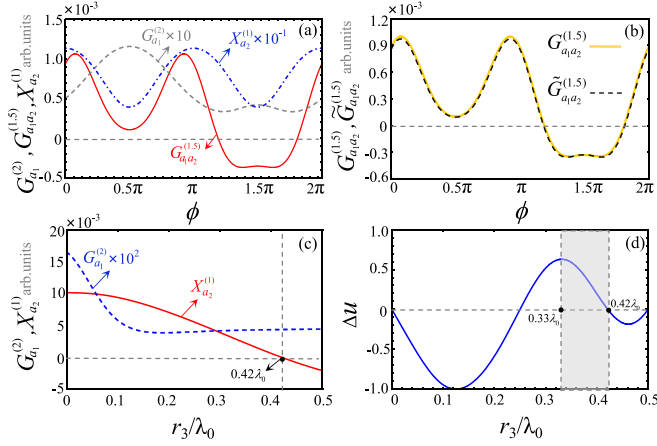
FIG. 7. (a) Angular distributions of $G_{a_1a_2}^{(1.5)}$ (red solid line), $G_{a_1}^{(2)} \times 10$ (gray dashed line), and $X_{a_2}^{(1)} \times 10^{-1}$ (blue dashed-dotted line) for $r_{12} = r_3 = 0.3\lambda_0$. (b) Comparison of the angular distributions of the total intensity-field correlation $G_{a_1a_2}^{(1.5)}$ calculated by Eq. (E3) (yellow solid line) with that of the dominant contribution $\tilde{G}_{a_1a_2}^{(1.5)}$ (black dashed line) given by Eq. (33) for $r_{12} = r_3 = 0.3\lambda_0$. (c) The quadrature squared signal $X_{a_2}^{(1)}$ (red solid line) and the two-photon correlation $G_{a_1}^{(2)}$ (blue dashed line) varying with the distance r_3 for $r_{12} = 0.3\lambda_0$ and $\phi = 3\pi/2$. (d) The function $\Delta u(r_3) = [u(r_3, 3\pi/2)]^2 - [u(r_3, \pi/2)]^2$ varying with the distance r_3 for $r_{12} = 0.3\lambda_0$. All the other parameters in (a)–(d) are the same as in Fig. 6.

the unidirectional nonclassical correlations in the direction of the central vertical line of the axis of the driven two-emitter subsystem.

In order to get a better insight into the origin of these nonclassical signals, in Fig. 7(a), we further compare the angular distributions of the relevant correlation functions for $x = 0$. This comparison reveals that the nonclassical peaks around $\phi = 0$ (2π) and π predict the directions in which the intensity-field correlation is significantly enhanced [see red solid line in Fig. 7(a)]. Whereas the extra nonclassical peak in the direction $\phi = 3\pi/2$ is derived from three aspects, including the suppression of $X_{a_2}^{(1)}$, the destructive interference of $G_{a_1}^{(2)}$, and the enhancement of $(G_{a_1a_2}^{(1.5)})^2$, as shown in Fig. 7(a). Let us first examine the angular distribution of the intensity-field correlation. For a properly large negative laser detuning, although the full solution of $G_{a_1a_2}^{(1.5)}$ arises from the contributions of all the populations and atomic coherences, the value of $G_{a_1a_2}^{(1.5)}$ is predominantly contributed from the atomic coherences ρ_{24} and ρ_{42}, as illustrated in Fig. 7(b), in which the full analytical expression of $G_{a_1a_2}^{(1.5)}$ is given by Eqs. (E3) and (E4) in Appendix E. We label the dominant component of $G_{a_1a_2}^{(1.5)}$ as $\tilde{G}_{a_1a_2}^{(1.5)}$, which is calculated as

$$
\begin{aligned}
\tilde{G}_{a_1a_2}^{(1.5)} &= 2\text{Re}\big[\rho_{42}\mathcal{C}_{5,1_{a_1},0_{a_2}}^{(2)*}\mathcal{C}_{5,1_{a_1},1_{a_2}}^{(4)} + \rho_{24}\mathcal{C}_{6,1_{a_1},0_{a_2}}^{(4)*}\mathcal{C}_{6,1_{a_1},1_{a_2}}^{(2)}\big] \\
&= 16A_1B_1\xi^3|\rho_{24}|(1 + 2\sin^2\psi_{12})\cos(\psi_3 + \pi/2).
\end{aligned}
\tag{33}
$$

This result suggests once again that the geometrical modulation effects of the driven two-emitter subsystem and the undriven emitter are completely separated. For the driven two-emitter subsystem, the propagation directions of emitted the photons that optimally enhance the value of $(G_{a_1a_2}^{(1.5)})^2$

are subject to the relation $\sin\psi_{12} = \pm 1$, which implies the restriction on distance $r_{12} \geqslant |n + 1/2|\lambda_0 \geqslant \lambda_0/2$. However, for a smaller distance $r_{12} < \lambda_0/2$, although the perfectly optimal values of the term $\sin\psi_{12}$, i.e., $\sin\psi_{12} = \pm 1$, cannot be achieved for all directions, the distinct nonclassicality can still be observed in the two symmetrical directions $\phi = 0$ and π, which maximize the term $\sin^2\psi_{12}$ and give rise to a pair of symmetrical nonclassical peaks in Fig. 6(c). Whereas the rotationally asymmetrical nonclassicality corresponding to the isolated peak in the direction $\phi = 3\pi/2$ is the modulation effect of the undriven emitter, including the destructive interference of two-photon emissions in the three-body cooperative mode a_1 around the direction $\phi = 3\pi/2$ [see the gray dashed line in Fig. 7(a)], and the asymmetrical intensity-field correlation with the geometrical modulation function $u(r_3, \phi) = \cos(\psi_3 + \pi/2)$, whose optimally negative value appears at $\phi = 3\pi/2$. Before discussing the feasibility of using the auxiliary emitter to further enhance the nonclassical signal at $\phi = 3\pi/2$, we examine in Fig. 7(c) the behaviours of $X_{a_2}^{(1)}$ and $G_{a_1}^{(2)}$ varying with the distance r_3 for $r_{12} = 0.3\lambda_0$ and $\phi = 3\pi/2$. Under the given parameters, the critical distance corresponding to the sign change of $X_{a_2}^{(1)}$ is determined as $r_3 \approx 0.42\lambda_0$. Meanwhile, it can be seen that the two-photon probability $G_{a_1a_2}^{(2)}$ at $\phi = 3\pi/2$ is stable in the range of $r_3 \in [0.15\lambda_0, 0.5\lambda_0]$ (see the blue dashed line in Fig. 7(c)), which means that the destructive interference of two-photon emissions that is conducive to achieve prominent nonclassical signal can persist in this direction. Given this feature, we explore in Fig. 7(d) the degree of asymmetry of the intensity-field correlation signal in the direction perpendicular to the axis of the two-emitter subsystem by introducing the function $\Delta u(r_3) = [u(r_3, 3\pi/2)]^2 - [u(r_3, \pi/2)]^2$. Based on the result in Fig. 7(c) that the quadrature squared signal is monotonically decreased to zero when the distance r_3 is increased to approach the critical value $0.42\lambda_0$, the extremely large positive value of the violation of degree $\mathcal{R}_{a_1a_2}^{(1.5)}$ can be achieved. Therefore a possible region for generating remarkable value of $\mathcal{R}_{a_1a_2}^{(1.5)}$ is determined as $r_3 \in [0.33\lambda_0, 0.42\lambda_0]$ (the shaded region in Fig. 7(d)) for $r_{12} = 0.3\lambda_0$, where the lower boundary $0.33\lambda_0$ corresponds to the maximum value of $\Delta u(r_3)$, as shown in Fig. 7(d). Based on the discussed strategy of using the undriven emitter to achieve the directional nonclassicality in the direction perpendicular to the axis of the driven two-emitter subsystem, we present in Fig. 8 the angular distributions of $\mathcal{R}_{a_1a_2}^{(1.5)}$ for different values of r_{12}, in which $r_3 = 0.38\lambda_0$ is determined for $r_{12} = 0.3\lambda_0$ according to the above analysis, corresponding to Fig. 8(a). Meanwhile we should point out that the parameters in Fig. 8 have ensured that the value of $X_{a_2}^{(1)}$ is positive in all directions, thus the criterion of $\mathcal{R}_{a_1a_2}^{(1.5)} > 1$ in determining the nonclassical correlations is valid.

In order to shed more light on the intensity-field correlations in detecting the directional two-mode nonclassicality, it is also worthwhile to point out that another version of the Cauchy-Schwarz inequality is also effective, which takes the form [47]

$$
n_{ab}^{(1.5)} = \frac{|\langle a^\dagger ab\rangle|^2}{\langle a^{\dagger 2}a^2\rangle\langle b^\dagger b\rangle} \leqslant 1,
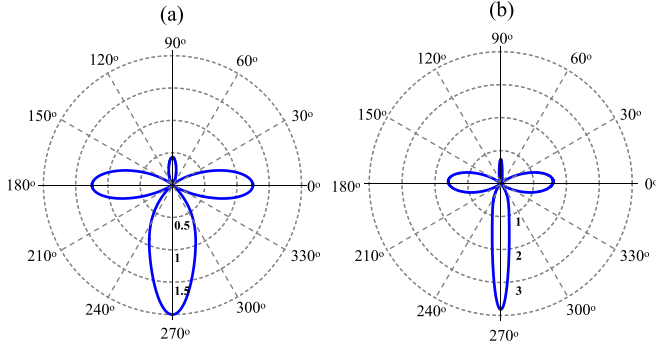\tag{34}
$$

FIG. 8. Angular distributions of the violation degree of the Cauchy-Schwarz inequality $\mathcal{R}_{a_1 a_2}^{(1.5)}$ for the distances (a) $r_{12} = 0.3\lambda_0$ and $r_3 = 0.38\lambda_0$, and (b) $r_{12} = 0.5\lambda_0$ and $r_3 = 0.35\lambda_0$. All the other parameters in (a) and (b) are the same as in Fig. 6.

and $\eta_{ab}^{(1.5)} > 1$ indicates two-mode nonclassical correlations. In Fig. 9, we present the angular distributions of the function $\eta_{a_1 a_2}^{(1.5)}$ for our system. One can see that, under the given parameters, four lobes can be observed around the directions $\phi = \pi/3$, $2\pi/3$, $4\pi/3$, and $5\pi/3$, in which the two distinct lobes mark the nonclassical correlations with concentrated directionality. These four lobes exactly predict the directions in which the single-photon emission in mode a_2 is suppressed. Although their directions are rotationally symmetrical, the magnitudes are in sharp contrast, which results from the rotational asymmetry of the intensity-field correlator $\langle a_1^\dagger a_1 a_2 \rangle$.

Now let us discuss some physical information conveyed by the intensity-field correlation function, although it cannot be understood as the probability of photon detections. The analytical result in Eq. (33) indicates that the intensity-field correlator $\langle a_1^\dagger a_1 a_2 \rangle$ essentially reflects the quantum coherence between the single-photon state $|5, 1_{a_1}, 0_{a_2}\rangle$ and the two-photon state $|5, 1_{a_1}, 1_{a_2}\rangle$, and the quantum coherence between the states $|6, 1_{a_1}, 0_{a_2}\rangle$ and $|6, 1_{a_1}, 1_{a_2}\rangle$, in which the two correlated photon states belong to different cascaded emission groups coupled by the effective dipole-dipole interaction $\Omega_+^{(dd)}$, as illustrated by the black dashed arrows in Fig. 10. Hence the intensity-field correlation signal conveys the in-
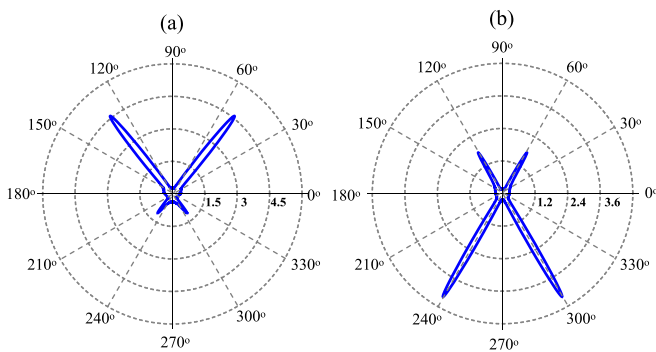

FIG. 9. Angular distributions of the violation degree of the Cauchy-Schwarz inequality $\eta_{a_1 a_2}^{(1.5)}$ for the distances (a) $r_{12} = 0.8\lambda_0$, $r_3 = 0.4\lambda_0$, and (b) $r_{12} = \lambda_0$, $r_3 = 0.1\lambda_0$. Other parameters are $\Omega = 100\gamma$, $\Delta = -150\gamma$, $\kappa = 20\gamma$, $\mu = 0.8$, $\theta_l = \pi/2$, $\theta_d = 0$, $\vartheta_3 = \pi/2$, $\delta_1 = \bar{\Omega}$, and $\delta_2 = 0$.
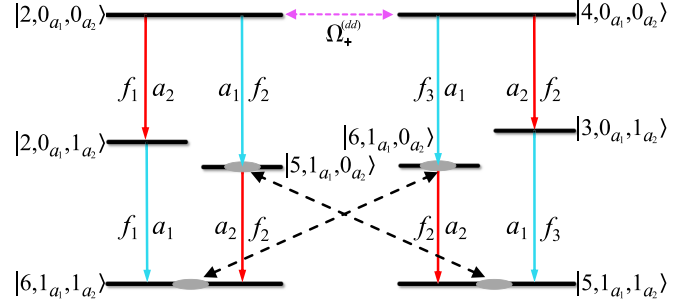

FIG. 10. Dominant two-photon cascaded emissions of the two-mode fields (a_1, a_2), in which the two cascaded emission groups are triggered by the initial dressed atomic states $|2\rangle$ and $|4\rangle$, respectively. Quantum coherence between the single-photon state $|5, 1_{a_1}, 0_{a_2}\rangle$ $(|6, 1_{a_1}, 0_{a_2}\rangle)$ in the cascaded emission group triggered by the state $|2\rangle$ $(|4\rangle)$ and the two-photon state $|5, 1_{a_1}, 1_{a_2}\rangle$ $(|6, 1_{a_1}, 1_{a_2}\rangle)$ in the cascaded emission group triggered by the initial dressed atomic state $|4\rangle$ $(|2\rangle)$ is revealed by the intensity-field correlation function $G_{a_1 a_2}^{(1.5)}$.

formation that the three-body cooperative mode a_1 emitted from the transition $|4\rangle \xrightarrow{a_1} |6\rangle$, for example, not only participates in a pair of two-photon cascaded transitions with opposite emission orderings, i.e., $|4\rangle \xrightarrow{a_1} |6\rangle \xrightarrow{a_2} |5\rangle$ and $|4\rangle \xrightarrow{a_2} |3\rangle \xrightarrow{a_1} |5\rangle$, but also regulates another pair of two-photon transitions $|2\rangle \xrightarrow{a_2} |2\rangle \xrightarrow{a_1} |6\rangle$ and $|2\rangle \xrightarrow{a_1} |5\rangle \xrightarrow{a_2} |6\rangle$ established between the driven two-emitter subsystem. Obviously, the quantum coherence of photon states is the wavelike property of radiation. In this sense, the intensity-field correlation function seems to be complementary to the familiar intensity-intensity correlation function, which conveys the information about the particlelike property of radiation by probing the populations of photon states. In other words, the intensity-intensity correlation function and the intensity-field correlation function in our quantum filtering system display the directionality of nonclassical properties of collective stimulated radiation from different perspectives, including the particle property and the coherence of frequency-resolved resonance fluorescence.

C. Geometry-dependent frequency-resolved entanglement

We now proceed to explore the feasibility of generating the frequency-resolved entangled emissions along some specific directions in our system. In Refs. [76,77], Hillery and Zubairy proposed the inequalities

$$\langle a^{\dagger m} a^m b^{\dagger n} b^n \rangle < |\langle a^{\dagger m} b^n \rangle|^2,$$
$$\langle a^{\dagger m} a^m \rangle \langle b^{\dagger n} b^n \rangle < |\langle a^m b^n \rangle|^2, \quad (35)$$

which can be applied to test higher-order two-mode entanglement. For the case of the lowest order ($m = n = 1$), these criteria involve the correlators $\langle a^\dagger b \rangle$ and $\langle ab \rangle$. In our quantum filtering system of two-photon filtering dynamics, we get

$$\langle a^\dagger b \rangle = \sum_k \langle k, 0_a, 1_b | \rho_{S,ab} | k, 1_a, 0_b \rangle,$$
$$\langle ab \rangle = \sum_k \langle k, 0_a, 0_b | \rho_{S,ab} | k, 1_a, 1_b \rangle. \quad (36)$$

Considering that the single-photon transitions of two different modes triggered by a common initial dressed state will
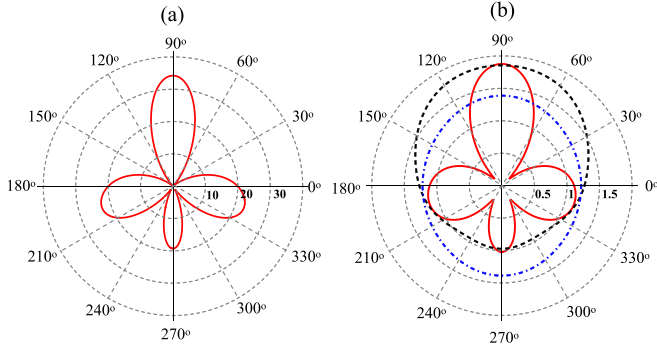
FIG. 11. Angular distributions of (a) the entanglement parameter $E_{a_1 a_3}$ and (b) the relevant correlation functions. In (b), $|G_{a_1 a_3}^{(0,2)}| \times 10^2$, $5G_{a_1}^{(1)} \times 10^2$, and $5G_{a_3}^{(1)} \times 10^2$ correspond to the red solid curve, the black dashed curve, and the blue dashed-dotted curve, respectively. Other parameters are $r_{12} = 0.4\lambda_0$, $r_3 = 0.35\lambda_0$, $\Omega = 100\gamma$, $\Delta = -150\gamma$, $\kappa = 20\gamma$, $\mu = 0.8$, $\theta_l = \pi/2$, $\theta_d = 0$, $\vartheta_3 = \pi/2$, and $\delta_1 = -\delta_3 = \bar{\Omega}$.

fall into different dressed states, we have $\langle a_1^\dagger a_2 \rangle = \langle a_1^\dagger a_3 \rangle = 0$ in our system. If the other correlator $\langle ab \rangle$ is nonzero, it requires that the cascaded two-mode two-photon transitions cannot affect the dressed atomic state of zero-photon and two-photon states. Obviously, in our system, the two-mode sideband fields (a_1, a_3) satisfy this requirement due to $\nu_1 + \nu_3 = 2\omega_L$, and also satisfy $\langle a_1 \rangle = \langle a_3 \rangle = 0$. Therefore the sideband filtered modes a_1 and a_3 are entangled if

$$E_{a_1 a_3} = \frac{|G_{a_1 a_3}^{(0,2)}|^2}{G_{a_1}^{(1)} G_{a_3}^{(1)}} > 1, \tag{37}$$

with $G_{a_1 a_3}^{(0,2)} = \langle a_1 a_3 \rangle$, $G_{a_1}^{(1)} = \langle a_1^\dagger a_1 \rangle$, and $G_{a_3}^{(1)} = \langle a_3^\dagger a_3 \rangle$. The superscript "(0,2)" represents that the correlator $\langle a_1 a_3 \rangle$ refers to "(field)^2" without negative-frequency field component. It is worth mentioning that this condition of two-mode entanglement reminds us of the definition of anomalous cross-correlation function [52,53]

$$g_{ab}^{(0,2)} = \frac{|\langle ab \rangle|}{\sqrt{\langle a^\dagger a \rangle \langle b^\dagger b \rangle}}. \tag{38}$$

Thus the two-mode entanglement can be detected by an alternative form, i.e., the anomalous correlation $g_{ab}^{(0,2)} > 1$. For many radiation processes, anomalous correlation has not received much attention. However, an interesting question may arise in our system —— what is the physical information the anomalous correlation conveys via the directionality of entanglement.

In Fig. 11, we present the single-point angular distributions of $E_{a_1 a_3}$ and the relevant correlation functions. It is seen that the frequency-resolved two-mode entanglement in Fig. 11(a) is strongly dependent on the unnormalized anomalous correlation function $G_{a_1 a_3}^{(0,2)}$ [red solid curve in Fig. 11(b)]. The full analytical expression of the unnormalized anomalous correlation function $G_{a_1 a_3}^{(0,2)}$ is given by Eqs. (E5) and (E6) in Appendix E by considering the contributions of all the populations and atomic coherences. Based on the full solution of $G_{a_1 a_3}^{(0,2)}$, we can examine that the main contribution of the
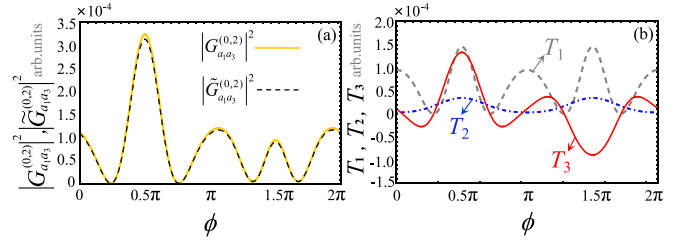

FIG. 12. (a) Comparison of the angular distributions of the magnitude squared of the total anomalous correlation $|G_{a_1 a_3}^{(0,2)}|^2$ calculated by Eq. (E5) (yellow solid line) with that of the main component $|\tilde{G}_{a_1 a_3}^{(0,2)}|^2$ (black dashed line) given by Eq. (40). (b) Angular distributions of the functions T_1 (gray dashed line), T_2 (blue dashed-dotted line), and T_3 (red solid line). All the parameters are the same as in Fig. 11.

anomalous correlation corresponds to

$$\tilde{G}_{a_1 a_3}^{(0,2)} = \rho_{22} \mathcal{C}_{2,1_{a_1},1_{a_3}}^{(2)} + \rho_{42} \mathcal{C}_{2,1_{a_1},1_{a_3}}^{(4)}, \tag{39}$$

and its contribution to the total anomalous correlation function $G_{a_1 a_3}^{(0,2)}$ is shown in Fig. 12(a). Then we obtain the magnitude squared of the main anomalous correlation as

$$|\tilde{G}_{a_1 a_3}^{(0,2)}|^2 = T_1 + T_2 + T_3, \tag{40}$$

with the following three parts:

$$T_1 = |\rho_{22} \mathcal{C}_{2,1_{a_1},1_{a_3}}^{(2)}|^2,$$
$$T_2 = |\rho_{42} \mathcal{C}_{2,1_{a_1},1_{a_3}}^{(4)}|^2,$$
$$T_3 = 2\mathrm{Re}\left[\rho_{22} \rho_{42} \mathcal{C}_{2,1_{a_1},1_{a_3}}^{(2)*} \mathcal{C}_{2,1_{a_1},1_{a_3}}^{(4)}\right]. \tag{41}$$

Figure 12(b) shows the angular distributions of T_1 (gray dashed line), T_2 (blue dashed-dotted line), and T_3 (red solid line). One can see from Eqs. (39)–(41) that the anomalous correlation conveys the information of the two-photon cascaded emissions that are resonant with two dressing photons, including the independent cascaded emissions and the interference of cascaded emissions. The components T_1 and T_2 are similar in form to that of the two-photon probability components $\mathcal{P}_{22}$ and $\mathcal{P}_{44}$ in Eq. (26), except that their magnitudes might be different. Thus the symmetry of T_1 and T_2 can be also traced back to the physical origin of the symmetry of $\mathcal{P}_{22}$ and $\mathcal{P}_{44}$, i.e., the symmetrical two-photon cascaded emissions resolved by the filters. Whereas the component T_3 reflects the geometrical modulation effect of the auxiliary undriven emitter on the dressed two-body radiating source, which leads to the frequency-resolved two-mode entanglement for different sideband fields along a specific emission direction. Furthermore, Eq. (39) tells us that the anomalous correlation $G_{a_1 a_3}^{(0,2)}$ still provides the directionality of nonclassical properties of resonance fluorescence by conveying the information about the quantum coherences of photon states, but what it mainly reveals is the coherence between the zero-photon state $|2, 0_{a_1}, 0_{a_3}\rangle$ and the target two-photon state $|2, 1_{a_1}, 1_{a_3}\rangle$ belonging in a common cascaded emission group, and the coherence between the zero-photon state $|2, 0_{a_1}, 0_{a_3}\rangle$ and the target two-photon state $|4, 1_{a_1}, 1_{a_3}\rangle$ belonging in different cascaded emission groups. In other words, the correlator

$\langle a_1 a_3 \rangle$ is related to two-photon coherence [78]. Obviously, this physical information is different from the intensity-field correlation function discussed in the above. It is also worth mentioning that anomalous correlation function has been discussed in collective resonance fluorescence of multiatom system [53], in which the information about higher-order resonance can be conveyed by the anomalous correlation function of electric dipole radiation fields.

D. Comparisons with a strongly driven two-body quantum antenna

Before finishing our discussions, we would like to make some brief comparisons between the three-body quantum antenna and a strongly driven two-body quantum antenna, in which both the two identical two-level quantum emitters are strongly dressed. To our knowledge, only a few researches have been devoted to the directional properties of the spectral correlations in two-atom resonance fluorescence. We hope that these comparisons can provide some complementary results for strongly driven two-atom systems.

The strongly driven two-body quantum antenna can be recovered from our system by setting the distance r_3 to infinity, thus Ω_{13} and Ω_{23} are negligible. However, considering the rotational symmetry of the angular distribution of radiation in the dressed two-body system, in order to ensure the rationality of the comparisons, the three-body quantum antenna should be linear and symmetrical, in which the auxiliary emitter 3 is located at the center point between the emitters 1 and 2, i.e., $r_3 = 0$. In Fig. 13, we compare the angular distributions of the nonclassical signals of the linear symmetrical three-body quantum antenna (red solid curves) with that of the strongly dressed two-body quantum antenna (blue dashed curves). It can be seen from Figs. 13(b) and 13(d) that the values of $\mathcal{R}_{a_1 a_3}^{(2)}$ and $E_{a_1 a_3}$ are weakened by the presence of the emitter 3, however, the lobes of the two systems predict the coincident directions of nonclassical correlations. In addition, Figs. 13(a) and 13(c) indicate that the dipole-dipole interactions between the undriven emitter and the driven two-emitter subsystem provide some positive effects on the nonclassical correlations between the central-frequency and the higher-frequency photons. For instance, Fig. 13(a) shows that the emitter 3 further increases the value of $\mathcal{R}_{a_1 a_2}^{(2)}$, and Figs. 13(c) and 13(e) indicate that the signals $\eta_{a_1 a_2}^{(1.5)}$ and $\mathcal{D}_{a_1 a_2}^{(1.5)}$ of the two-body quantum antenna cannot display nonclassical correlations in all directions (the blue dashed curve in Fig. 13(c) corresponds to $\eta_{a_1 a_2}^{(1.5)} \times 5$). However, the three-body quantum antenna not only improves these signals to reach the nonclassical levels, but also produces strong directionality with narrow nonclassical lobes. These improvements are originated from the nonzero signal components related to the dressed population ρ_{44} and the atomic coherence ρ_{24} in the three-body quantum antenna, which should have been zero in the two-body quantum antenna. The dressed state $|4\rangle$ is related to the excited state of the auxiliary emitter [see Eqs. (A1)–(A3) in Appendix A], which is populated by the electric dipole-dipole interactions between the driven two-emitter subsystem and the auxiliary emitter.
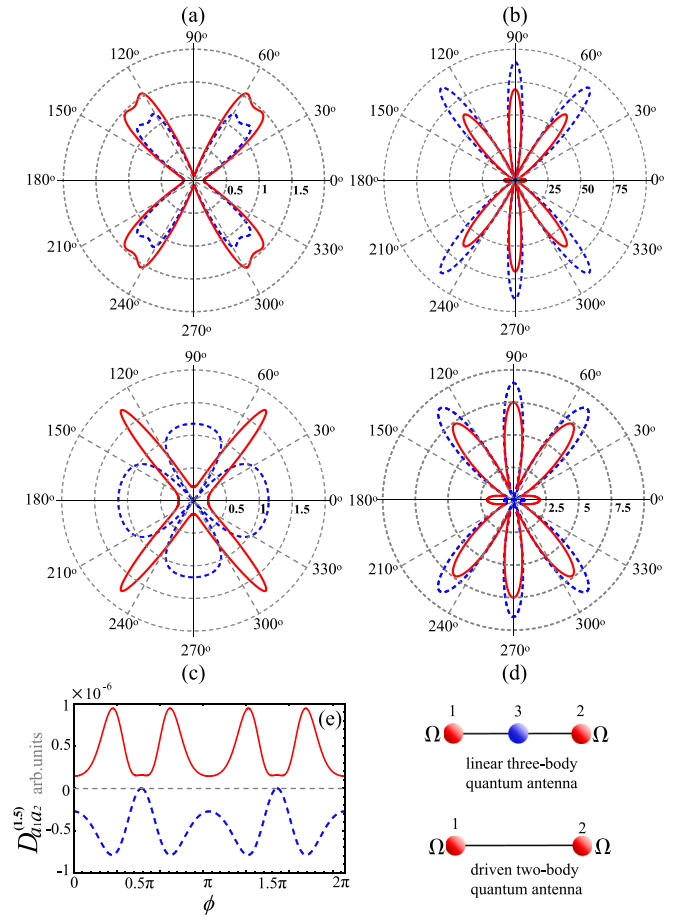

FIG. 13. Comparisons of the angular distributions of the parameters (a) $\mathcal{R}_{a_1 a_2}^{(2)}$, (b) $\mathcal{R}_{a_1 a_3}^{(2)}$, (c) $\eta_{a_1 a_2}^{(1.5)}$, (d) $E_{a_1 a_3}$, and (e) $\mathcal{D}_{a_1 a_2}^{(1.5)}$ of the symmetrical linear three-body quantum antenna (red solid curves) with that of the strongly driven two-body quantum antenna (blue dashed curves). In (c), the blue dashed curve corresponds to $\eta_{a_1 a_2}^{(1.5)} \times 5$. The parameters are $r_{12} = 0.8\lambda_0$, $\Omega = -\Delta = 100\gamma$, $\kappa = 20\gamma$, $\mu = 0.8$, $\theta_l = \pi/2$, $\theta_d = 0$, $\delta_1 = -\delta_3 = \bar{\Omega}$, and $\delta_2 = 0$.

V. SUMMARY

By constructing a quantum filtering system, we have investigated the directionality of spectrally correlated nonclassical properties of collective resonance fluorescence radiated from a three-body quantum antenna. The quantum antenna is composed of two resonantly, strongly driven identical two-level electric dipolar emitters, plus an auxiliary undriven emitter, whose resonant transition corresponds to the higher-frequency sideband of the collective resonance fluorescence of the two driven emitters. In far-field zone, three single-mode quantum cavities are applied to filter the photons from the three spectral components respectively. In the limit of large passband width, the calculations of the quantum filtering dynamics of the combined system have been carried out analytically in the frame of cascaded quantum system.

By correlating the target cavity modes, we have found that the two types of spectral combinations including the three-body collective mode allow for strongly directional nonclassical correlations. On the one hand, when the two opposite sidebands are correlated with each other, the giant violation of

the Cauchy-Schwarz inequality related to intensity-intensity correlation functions can be achieved with well-defined directions, and the frequency-resolved two-mode entanglement along a specific direction can be detected by anomalous correlation function. The physical origin can be attributed to the atomic coherent effects arising from the electric dipole-dipole interactions between the undriven emitter and the dressed two-body radiating source. Specifically, the interatomic interactions couple different cascaded emission groups, in which the asymmetrical two-photon cascaded transitions are constructed. On the other hand, the prominent directionality of nonclassical correlations can be also generated by correlating a central-frequency photon and a higher-frequency photons, which is identified through the violation of the Cauchy-Schwarz inequality related to intensity-field correlation. The intensity-field correlation function for this spectral combination displays rotational asymmetry by revealing the quantum coherences between the single-photon states and the two-photon states in different cascaded emission groups. Therefore these various frequency-resolved correlation functions characterize the spatial asymmetry of nonclassical properties of the collective resonance fluorescence from different perspectives, including the particlelike properties and the quantum coherences of the filtered photons. In addition, we have examined the feasibility of using the auxiliary emitter to produce the optimal nonclassical signals along a specific emission direction. Finally, we have compared our system with a strongly driven two-atom quantum antenna, and have found that the presence of the auxiliary undriven emitter can improve some signals in the two-atom system to reach nonclassical levels with strong directionality.

Our investigation provides a theoretical scheme for preparing the frequency-resolved nonclassical light with strong directionality. We hope that the proposed scheme could be helpful for the construction of quantum radars to further realize using the nonclassical light with angular and spectral resolutions to probe another target quantum systems.

APPENDIX A: DRESSED STATES AND GEOMETRY-DEPENDENT ELECTRIC DIPOLE RADIATION OPERATORS

In this Appendix, we present the representation transformation between the three-body bare states and the dressed atomic states. Then, we give the explicit expressions of the geometry-dependent electric dipole radiation operators in Eq. (6).

Firstly, we define the three-body bare states as

$$
\begin{aligned}
|\psi_1\rangle &= |e_1, g_2, g_3\rangle, & |\psi_2\rangle &= |e_1, e_2, g_3\rangle, \\
|\psi_3\rangle &= |e_1, g_2, e_3\rangle, & |\psi_4\rangle &= |e_1, e_2, e_3\rangle, \\
|\psi_5\rangle &= |g_1, g_2, g_3\rangle, & |\psi_6\rangle &= |g_1, e_2, g_3\rangle, \\
|\psi_7\rangle &= |g_1, g_2, e_3\rangle, & |\psi_8\rangle &= |g_1, e_2, e_3\rangle.
\end{aligned} \tag{A1}
$$

By diagonalizing the Hamiltonian $H_S + H_L$ under the condition $\Delta_1 = \Delta_2 = \Delta$ and $\Omega(\mathbf{r}_1) = \Omega(\mathbf{r}_2) = \Omega$, one can obtain the Hamiltonian of the laser-dressed three-body quantum antenna $\tilde{H}_S$, which is spaced by the dressed-state basis $\{|k\rangle\}$ $k \in \{1, 2, \ldots, 8\}$. The representation transformation between the dressed states and the three-body bare states can be given by the vector form $\mathbf{a} = \mathbf{U}\mathbf{b}$, where the dressed-state vector and the bare-state vector are defined as

$$
\mathbf{a} = (|1\rangle, |2\rangle, \ldots, |7\rangle, |8\rangle)^{\mathrm{T}},
$$
$$
\mathbf{b} = (|\psi_1\rangle, |\psi_2\rangle, \ldots, |\psi_7\rangle, |\psi_8\rangle)^{\mathrm{T}}, \tag{A2}
$$

respectively, with the symbol "T" denoting the transpose of matrix, and the matrix $\mathbf{U}$ is the representation transformation matrix and is given by

$$
\mathbf{U} = \begin{pmatrix}
0 & 0 & cs & c^2 & 0 & 0 & s^2 & cs \\
cs & c^2 & 0 & 0 & s^2 & cs & 0 & 0 \\
0 & 0 & \frac{1}{\sqrt{2}} & 0 & 0 & 0 & 0 & -\frac{1}{\sqrt{2}} \\
0 & 0 & \frac{c^2-s^2}{\sqrt{2}} & -\sqrt{2}cs & 0 & 0 & \sqrt{2}cs & \frac{c^2-s^2}{\sqrt{2}} \\
\frac{1}{\sqrt{2}} & 0 & 0 & 0 & 0 & -\frac{1}{\sqrt{2}} & 0 & 0 \\
\frac{c^2-s^2}{\sqrt{2}} & -\sqrt{2}cs & 0 & 0 & \sqrt{2}cs & \frac{c^2-s^2}{\sqrt{2}} & 0 & 0 \\
0 & 0 & cs & -s^2 & 0 & 0 & -c^2 & cs \\
cs & -s^2 & 0 & 0 & -c^2 & cs & 0 & 0
\end{pmatrix}. \tag{A3}
$$

For the condition of higher-frequency sideband resonance, i.e., $\Delta_3 = \bar{\Omega}$, we find that the coherent dipole-dipole interaction between the two laser-driven emitters described by the Hamiltonian $H_{12} = \Omega_{12}(S_1^+ S_2^- + S_2^+ S_1^-)$ leads to the level disturbances of the dressed states after transforming H_{12} into the dressed-state representation $\tilde{H}_{12}$ and neglecting rapidly oscillating terms. Thus

the Hamiltonian $\tilde{H}_0$ in Eq. (9) is given by $\tilde{H}_0 = \tilde{H}_S + \tilde{H}_{12}$, where

$$\tilde{H}_S = \sum_k \Omega_k^{(0)} |k\rangle\langle k|, \qquad \tilde{H}_{12} = \sum_k \delta\Omega_k |k\rangle\langle k|, \tag{A4}$$

with the free energies of the dressed states

$$\Omega_1^{(0)} = -\Omega_8^{(0)} = \frac{3\bar{\Omega}}{2},$$

$$\Omega_2^{(0)} = \Omega_3^{(0)} = \Omega_4^{(0)} = \frac{\bar{\Omega}}{2},$$

$$\Omega_5^{(0)} = \Omega_6^{(0)} = \Omega_7^{(0)} = -\frac{\bar{\Omega}}{2}, \tag{A5}$$

and the level shifts

$$\delta\Omega_3 = \delta\Omega_5 = -\Omega_{12},$$

$$\delta\Omega_4 = \delta\Omega_6 = 2B_2^2 \Omega_{12},$$

$$\delta\Omega_1 = \delta\Omega_2 = \delta\Omega_7 = \delta\Omega_8 = B_1^2 \Omega_{12}. \tag{A6}$$

Therefore the total energy distribution of the dressed states in Eq. (9) is given by $\Omega_k = \Omega_k^{(0)} + \delta\Omega_k$.

In terms of the dressed states, we can decompose the electric dipole radiation operator of each emitter according to the spectral components of the resonance fluorescence. For the identical driven emitters 1 and 2, we have the decompositions

$$S_1^- = S_1^{(1)} + S_2^{(1)} + S_3^{(1)},$$

$$S_2^- = S_1^{(2)} + S_2^{(2)} + S_3^{(2)}, \tag{A7}$$

where the higher-frequency, the central-frequency, and the lower-frequency spectral components are determined by

$$S_1^{(1,2)} = \frac{A_1}{\sqrt{2}} (\sigma_{41} + \sigma_{62} - \sigma_{74} - \sigma_{86} \mp \sigma_{31} \mp \sigma_{52} \mp \sigma_{73} \mp \sigma_{85}),$$

$$S_2^{(1,2)} = \frac{B_1}{\sqrt{2}} (\sigma_{11} + \sigma_{22} - \sigma_{77} - \sigma_{88} \pm \sigma_{34} \pm \sigma_{43} \pm \sigma_{56} \pm \sigma_{65}),$$

$$S_3^{(1,2)} = \frac{A_2}{\sqrt{2}} (\sigma_{47} + \sigma_{68} - \sigma_{14} - \sigma_{26} \pm \sigma_{13} \pm \sigma_{25} \pm \sigma_{37} \pm \sigma_{58}), \tag{A8}$$

respectively. However, the electric dipole radiation operator of the undriven emitter 3 is

$$S_3^- = S_1^{(3)} = \sigma_{21} + \sigma_{87} + \sigma_{64} + \sigma_{53}. \tag{A9}$$

In our scheme, the radiation field determined by $S_l^{(i)}$ is coupled with the corresponding cavity mode a_l unidirectionally along the propagation direction $\mathbf{k}_l$. By rearranging the collective electric dipole radiation operators according to the target spectral components, we thus obtain the geometry-dependent higher-frequency, the central-frequency, and the lower-frequency photon detection operators, respectively, as

$$\sigma_1 = \sum_{(k,k')} \mathcal{A}_{kk'}^{(a_1)} \sigma_{kk'} = \frac{A_1}{\sqrt{2}} [f_1(\mathbf{k}_1)(\sigma_{41} + \sigma_{62} - \sigma_{74} - \sigma_{86}) - f_2(\mathbf{k}_1)(\sigma_{31} + \sigma_{52} + \sigma_{73} + \sigma_{85})]$$

$$+ f_3(\mathbf{k}_1)(\sigma_{21} + \sigma_{87} + \sigma_{64} + \sigma_{53}),$$

$$\sigma_2 = \sum_{(k,k')} \mathcal{A}_{kk'}^{(a_2)} \sigma_{kk'} = \frac{B_1}{\sqrt{2}} [f_1(\mathbf{k}_2)(\sigma_{11} + \sigma_{22} - \sigma_{77} - \sigma_{88}) + f_2(\mathbf{k}_2)(\sigma_{34} + \sigma_{43} + \sigma_{56} + \sigma_{65})],$$

$$\sigma_3 = \sum_{(k,k')} \mathcal{A}_{kk'}^{(a_3)} \sigma_{kk'} = \frac{A_2}{\sqrt{2}} [f_1(\mathbf{k}_3)(\sigma_{47} + \sigma_{68} - \sigma_{14} - \sigma_{26}) + f_2(\mathbf{k}_3)(\sigma_{13} + \sigma_{37} + \sigma_{25} + \sigma_{58})], \tag{A10}$$

which correspond to Eq. (6). For convenience, we abbreviate the explicit expression of each geometry-dependent dipole operator in Eq. (A10) as $\sigma_l = \sum_{(k,k')} \mathcal{A}_{kk'}^{(a_l)} \sigma_{kk'}$ with the indexes $l \in \{1, 2, 3\}$ and $k, k' \in \{1, 2, \dots, 8\}$.

APPENDIX B: EQUATIONS OF MOTION AND STEADY-STATE SOLUTIONS FOR THE ATOMIC DENSITY MATRIX ELEMENTS

In this Appendix, we present the equations of motion and steady-state solutions for the reduced density matrix elements of the source with nonzero steady-state values.

In the condition of higher-frequency sideband resonance, we get two sets of degenerate dressed states $\{|2\rangle, |3\rangle, |4\rangle\}$ and $\{|5\rangle, |6\rangle, |7\rangle\}$ [see Eq. (A5)]. Furthermore, in the considered isosceles triangle configuration ($\gamma_{13} = \gamma_{23} = \gamma_r$, $\Omega_{13} = \Omega_{23} = \Omega_r$), the two-atom antisymmetric superposition states $|3\rangle$ and $|5\rangle$ are decoupled from the electric dipole-dipole interactions established between the dressed two-atom radiating source and the undriven auxiliary emitter. Therefore only the steady-state populations ρ_{kk} ($k \in \{1, 2, \ldots, 8\}$) and the atomic coherences ρ_{24}, ρ_{42}, ρ_{67}, and ρ_{76} are nonzero. When the density matrix element ρ_{88}, for example, is eliminated from the equations of motion, the dynamical evolution of this set of density matrix elements obey the inhomogeneous differential equation of the vector form

$$\frac{d}{dt}\mathbf{X} = \mathbf{MX} + \mathbf{C}, \tag{B1}$$

where the matrix of the density matrix elements $\mathbf{X}$ and the nonhomogeneous term are

$$\mathbf{X} = (\rho_{11}, \rho_{22}, \rho_{33}, \rho_{44}, \rho_{55}, \rho_{66}, \rho_{77}, \rho_{24}, \rho_{42}, \rho_{67}, \rho_{76})^{\mathrm{T}},$$
$$\mathbf{C} = (0, 0, 0, 0, \alpha_4, \alpha_3, 0, 0, 0, 0, 0)^{\mathrm{T}}, \tag{B2}$$

and the coefficient matrix $\mathbf{M}$ is given by

$$\mathbf{M} = \begin{pmatrix} -\beta_1 & 0 & \alpha_4 & \alpha_3 & 0 & 0 & 0 & 0 & 0 & 0 & 0 \\ \gamma & -\beta_2 & 0 & 0 & \alpha_4 & \alpha_3 & 0 & -\chi^* & -\chi & 0 & 0 \\ \alpha_2 & 0 & -\beta_3 & \alpha_5 & 0 & 0 & \alpha_4 & 0 & 0 & 0 & 0 \\ \alpha_1 & 0 & \alpha_5 & -\beta_4 & 0 & 0 & \alpha_3 & -\chi & -\chi^* & 0 & 0 \\ -\alpha_4 & \alpha_2-\alpha_4 & \gamma-\alpha_4 & -\alpha_4 & -(\beta_5+\alpha_4) & \alpha_5-\alpha_4 & -\alpha_4 & 0 & 0 & 0 & 0 \\ -\alpha_3 & \alpha_1-\alpha_3 & -\alpha_3 & \gamma-\alpha_3 & \alpha_5-\alpha_3 & -(\beta_6+\alpha_3) & -\alpha_3 & \alpha_6 & \alpha_6 & \chi^* & \chi \\ 0 & 0 & \alpha_2 & \alpha_1 & 0 & 0 & -\beta_7 & 0 & 0 & \chi & \chi^* \\ \alpha_6 & -\chi^* & 0 & -\chi & 0 & 0 & 0 & -\beta_{24} & 0 & -\alpha_3 & 0 \\ \alpha_6 & -\chi & 0 & -\chi^* & 0 & 0 & 0 & 0 & -\beta_{24}^* & 0 & -\alpha_3 \\ 0 & 0 & 0 & -\alpha_6 & 0 & \chi^* & \chi & -\alpha_1 & 0 & -\beta_{67} & 0 \\ 0 & 0 & 0 & -\alpha_6 & 0 & \chi & \chi^* & 0 & -\alpha_1 & 0 & -\beta_{67}^* \end{pmatrix}, \tag{B3}$$

with the coefficients

$$\alpha_1 = A_1^2(\gamma + \gamma_{12}), \qquad \alpha_2 = A_1^2(\gamma - \gamma_{12}), \qquad \alpha_3 = A_2^2(\gamma + \gamma_{12}), \qquad \alpha_4 = A_2^2(\gamma - \gamma_{12}),$$

$$\alpha_5 = B_1^2(\gamma - \gamma_{12}), \qquad \alpha_6 = \sqrt{2}A_1\gamma_r,$$

$$\beta_1 = (1 + 2A_1^2)\gamma, \qquad \beta_2 = 2A_1^2\gamma, \qquad \beta_3 = 2\gamma - \gamma_{12}, \qquad \beta_4 = 2\gamma + 2B_2^2\gamma_{12},$$

$$\beta_5 = \gamma - \gamma_{12}, \qquad \beta_6 = \gamma + 2B_2^2\gamma_{12}, \qquad \beta_7 = (1 + 2A_2^2)\gamma, \qquad \beta_8 = 2A_2^2\gamma,$$

$$\beta_{24} = \frac{1}{2}\big[(3 + \sqrt{2}B_2)\gamma + (A_1^2 + A_2^2)\gamma_{12}\big] + i(\Omega_2 - \Omega_4),$$

$$\beta_{67} = \frac{1}{2}\big[(3 - \sqrt{2}B_2)\gamma + (A_1^2 + A_2^2)\gamma_{12}\big] + i(\Omega_6 - \Omega_7), \qquad \chi = \frac{A_1}{\sqrt{2}}(\gamma_r + 2i\Omega_r). \tag{B4}$$

The steady-state solution of the matrix $\mathbf{X}$ can be expressed in component form as $\rho_{ij} = -\det[\mathbf{M}_{ij}]/\det[\mathbf{M}]$, where the symbol "det" represents the determinant of matrix, $\mathbf{M}_{ij}$ is the matrix obtained by replacing the column vector corresponding to the density matrix element ρ_{ij} in $\mathbf{M}$ by the inhomogeneous column vector $\mathbf{C}$. The nonzero steady-state populations and the coherences are fundamental in accessing the fluorescence emitted by the source, and the new populations in the diagonalized atomic representation, $\tilde{\rho}_{jj}$, can be calculated straightforwardly via the transformations (13) and (14).

APPENDIX C: PROOF OF THE FACTORIZATIONS IN EQUATIONS (17) AND (18)

In this Appendix, as an example, we give the detailed proof the factorization of two-mode correlators in Eqs. (17) and (18) in the limit of large filter linewidth. Similarly, the factorization of single-mode correlators can be also obtained through the same procedure.

1. General forms of the equations of motion for the atom-photon correlators

Let us work in the diagonalized atomic representation $\{|\tilde{j}\rangle\}$ to eliminate the steady-state atomic coherences (ρ_{24}, ρ_{42}, ρ_{67}, and ρ_{76}) temporarily. Thus the Hamiltonian of the source, $\tilde{H}_0 + \tilde{H}_I$ ($\tilde{H}_0 = \tilde{H}_S + \tilde{H}_{12}$), in Eq. (9) can be rewritten in the diagonalized

atomic representation as $\mathcal{H} = \mathcal{H}_0 + \mathcal{H}'_\gamma + \mathcal{H}''_\gamma$. The first part, $\mathcal{H}_0$, is transformed from the free dressed-state Hamiltonian $\tilde{H}_S$ in Eq. (A4), and thus takes the form

$$\mathcal{H}_0 = \sum_{j=1}^{8} \tilde{\Omega}_j^{(0)} \tilde{\sigma}_{jj}, \tag{C1}$$

with the unchanged free energies $\tilde{\Omega}_j^{(0)} = \Omega_j^{(0)}$. While the remaining parts $\mathcal{H}'_\gamma$ and $\mathcal{H}''_\gamma$ are transformed from $\tilde{H}_{12}$ in Eq. (A4) and $\tilde{H}_I$ in Eq. (9), respectively, and take the forms

$$\mathcal{H}'_\gamma = \sum_{j=1}^{8} \delta\tilde{\Omega}_j \tilde{\sigma}_{jj}, \qquad \mathcal{H}''_\gamma = (\varepsilon_1 \tilde{\sigma}_{24} + \varepsilon_1^* \tilde{\sigma}_{42}) + (\varepsilon_2 \tilde{\sigma}_{67} + \varepsilon_2^* \tilde{\sigma}_{76}), \tag{C2}$$

respectively, where the energy shifts of the diagonalized atomic states $\delta\tilde{\Omega}_j$ and the coherent coupling rates $\varepsilon_{1,2}$ are given by

$$
\begin{aligned}
\delta\tilde{\Omega}_1 &= \delta\Omega_1, & \delta\tilde{\Omega}_2 &= \delta\Omega_2 \sin^2\alpha_1 + \delta\Omega_4 \cos^2\alpha_1 + 2\Omega_+^{(dd)} \sin\alpha_1 \cos\alpha_1 \cos\phi_{24}, \\
\delta\tilde{\Omega}_3 &= \delta\Omega_3, & \delta\tilde{\Omega}_4 &= \delta\Omega_2 \cos^2\alpha_1 + \delta\Omega_4 \sin^2\alpha_1 - 2\Omega_+^{(dd)} \sin\alpha_1 \cos\alpha_1 \cos\phi_{24}, \\
\delta\tilde{\Omega}_5 &= \delta\Omega_5, & \delta\tilde{\Omega}_6 &= \delta\Omega_6 \sin^2\alpha_2 + \delta\Omega_7 \cos^2\alpha_2 + 2\Omega_+^{(dd)} \sin\alpha_2 \cos\alpha_2 \cos\phi_{67}, \\
\delta\tilde{\Omega}_8 &= \delta\Omega_8, & \delta\tilde{\Omega}_7 &= \delta\Omega_6 \cos^2\alpha_2 + \delta\Omega_7 \sin^2\alpha_2 - 2\Omega_+^{(dd)} \sin\alpha_2 \cos\alpha_2 \cos\phi_{67}, \\
\varepsilon_1 &= (\delta\Omega_4 - \delta\Omega_2) \sin\alpha_1 \cos\alpha_1 e^{i\phi_{24}}, & \varepsilon_2 &= (\delta\Omega_7 - \delta\Omega_6) \sin\alpha_2 \cos\alpha_2 e^{i\phi_{67}}.
\end{aligned}
\tag{C3}
$$

Obviously, the Hamiltonian $\mathcal{H}_0 + \mathcal{H}'_\gamma$ gives rise to the total free energies for the diagonalized atom by defining $\tilde{\Omega}_j = \tilde{\Omega}_j^{(0)} + \delta\tilde{\Omega}_j$. Considering that the geometrical scale of the quantum antenna and the condition of sideband resonance ensure that all the energy-level shifts $\delta\tilde{\Omega}_j$ and the coherent coupling rates $\varepsilon_{1,2}$ are within the natural linewidth of the single emitter, the perturbative Hamiltonians $\mathcal{H}'_\gamma$ and $\mathcal{H}''_\gamma$ give rise to the terms that are of the order of (or even less than) γ. With the help of the transformations (13) and (14), the damping terms in Eqs. (10) and (11) can be also transformed into the diagonalized atomic representation by reorganizing the photon detection operators in Eq. (A10) into the general form $\sigma_l = \sum_{(j,j')} \mathcal{B}_{jj'}^{(a_l)} \tilde{\sigma}_{jj'}$, where $l \in \{1, 2, 3\}$ and $j, j' \in \{1, 2, \ldots, 8\}$, and $\mathcal{B}_{jj'}^{(a_l)}$ is the transformed amplitude of the atomic transition $|\tilde{j}\rangle\langle\tilde{j'}|$ of generating the cavity mode a_l in the diagonalized atomic representation.

After transforming the master equation (8) into the diagonalized atomic representation, we can derive the equations of motion for the $(m + n + p + q)$th-order two-mode atom-photon correlators of the type $\langle a^{\dagger m} b^{\dagger p} b^q a^n \tilde{\sigma}_{rs} \rangle$ through the relation

$$
\begin{aligned}
\frac{d}{dt}\langle (a^{\dagger m} b^{\dagger p} b^q a^n \tilde{\sigma}_{rs})(t) \rangle &= \mathrm{Tr}\left[a^{\dagger m} b^{\dagger p} b^q a^n \tilde{\sigma}_{rs} \frac{d\tilde{\rho}}{dt} \right] \\
&= \mathrm{Tr}_{S,ab}\left[a^{\dagger m} b^{\dagger p} b^q a^n \tilde{\sigma}_{rs} \frac{d\tilde{\rho}_{S,ab}}{dt} \right],
\end{aligned}
\tag{C4}
$$

with $a, b \in \{a_1, a_2, a_3\}$ and $r, s \in \{1, 2, \ldots, 8\}$. Here we should point out that the dynamics of two-mode correlators are irrelevant with the presence of the remaining mode. For example, if we choose a_1 and a_2 as the target modes, the unidirectional dissipative coupling term of the remaining mode a_3 is $(\mathcal{L}_{SC}\tilde{\rho})_{a_3} = \sqrt{\mu\kappa\gamma}(\tilde{\sigma}_3\tilde{\rho}a_3^\dagger - a_3^\dagger\tilde{\sigma}_3\tilde{\rho} + a_3\tilde{\rho}\tilde{\sigma}_3^\dagger - \tilde{\rho}\tilde{\sigma}_3^\dagger a_3)$. We can easily examine that there is no contribution of $(\mathcal{L}_{SC}\tilde{\rho})_{a_3}$ to the equation of motion for the two-mode correlator $\langle a_1^{\dagger m} a_2^{\dagger p} a_2^q a_1^n \tilde{\sigma}_{rs} \rangle$. In other words, the correlator $\langle a_1^{\dagger m} a_2^{\dagger p} a_2^q a_1^n \tilde{\sigma}_{rs} \rangle$ is only related to the reduced density operator $\tilde{\rho}_{S,a_1a_2}$ after tracing out the mode a_3. Thus the calculations of the two-mode correlators for the target modes a_1 and a_2 are irrelevant with the remanding mode a_3 due to the lack of back action from the residual mode to the source. Similarly, the single-mode correlation properties are also unaltered by the other two modes.

Based on this fact, the equation of motion for the two-mode $(m + n + p + q)$th-order correlator $\langle a^{\dagger m} b^{\dagger p} b^q a^n \tilde{\sigma}_{rs} \rangle$ has the following recurrence form:

$$
\begin{aligned}
\frac{d}{dt}\langle a^{\dagger m} b^{\dagger p} b^q a^n \tilde{\sigma}_{rs} \rangle = &-\mathcal{K}_{rs}^{(m,p,q,n)} \langle a^{\dagger m} b^{\dagger p} b^q a^n \tilde{\sigma}_{rs} \rangle + \sum_{(i,i')} \mathcal{J}_{ii'}^{(rs)} \langle a^{\dagger m} b^{\dagger p} b^q a^n \tilde{\sigma}_{ii'} \rangle \\
&- \sqrt{\mu\kappa\gamma}\left(n \sum_j \mathcal{B}_{sj}^{(a)} \langle a^{\dagger m} b^{\dagger p} b^q a^{n-1} \tilde{\sigma}_{rj} \rangle + m \sum_j \mathcal{B}_{rj}^{(a)*} \langle a^{\dagger m-1} b^{\dagger p} b^q a^n \tilde{\sigma}_{js} \rangle \right) \\
&- \sqrt{\mu\kappa\gamma}\left(q \sum_j \mathcal{B}_{sj}^{(b)} \langle a^{\dagger m} b^{\dagger p} b^{q-1} a^n \tilde{\sigma}_{rj} \rangle + p \sum_j \mathcal{B}_{rj}^{(b)*} \langle a^{\dagger m} b^{\dagger p-1} b^q a^n \tilde{\sigma}_{js} \rangle \right),
\end{aligned}
\tag{C5}
$$

where the complex dissipation rate $\mathcal{K}_{rs}^{(m,p,q,n)}$ is

$$\mathcal{K}_{rs}^{(m,p,q,n)} = (m+n+p+q)\frac{\kappa}{2} - i[(m-n)\delta_a + (p-q)\delta_b + \tilde{\Omega}_r - \tilde{\Omega}_s], \tag{C6}$$

and the coefficient $\mathcal{J}_{ii'}^{(rs)}$ is the coupling coefficient of the atomic variable $\langle \tilde{\sigma}_{ii'}(t) \rangle$ coupled to $\langle \tilde{\sigma}_{rs}(t) \rangle$, which is the parameter of the source that is of the order of γ, i.e., γ, γ_{ij}, or Ω_{ij}. More specifically, the coupled terms $\langle a^{\dagger m} b^{\dagger p} b^q a^n \tilde{\sigma}_{ii'} \rangle$ $(i, i' \in \{1, 2, \ldots, 8\})$ in Eq. (C5) arise from the dynamical information of the source described by

$$\frac{d}{dt} \langle \tilde{\sigma}_{rs} \rangle = \sum_{(i,i')} \mathcal{J}_{ii'}^{(rs)} \langle \tilde{\sigma}_{ii'} \rangle, \tag{C7}$$

which is dominated by the superoperator

$$\mathcal{L}_\gamma \tilde{\rho}_S = -i[\mathcal{H}_\gamma'', \tilde{\rho}_S] + \tilde{\mathcal{L}}_S \tilde{\rho}_S \tag{C8}$$

via the relation $\frac{d}{dt} \langle \tilde{\sigma}_{rs} \rangle = \mathrm{Tr}[\tilde{\sigma}_{rs}(\mathcal{L}_\gamma \tilde{\rho}_S)]$. The explicit form the coefficient $\mathcal{J}_{ii'}^{(rs)}$ is given by the master equation for the corresponding atomic density matrix element presented in Appendix B. For example, the explicit form of the equation of motion for the two-mode second-order correlator $\langle a_1^\dagger a_2 \tilde{\sigma}_{11} \rangle$ is derived as

$$\frac{d}{dt} \langle a_1^\dagger a_2 \tilde{\sigma}_{11} \rangle = -[\kappa - i(\delta_1 - \delta_2) + \beta_1] \langle a_1^\dagger a_2 \tilde{\sigma}_{11} \rangle + \alpha_4 \langle a_1^\dagger a_2 \tilde{\sigma}_{33} \rangle + \alpha_3 \langle a_1^\dagger a_2 \tilde{\sigma}_{44} \rangle - \sqrt{\mu\kappa\gamma} \mathcal{B}_{11}^{(a_2)} \langle a_1^\dagger \tilde{\sigma}_{11} \rangle, \tag{C9}$$

in which the explicit forms of the coefficients β_1, α_3, and α_4 are given by Eq. (B4), and $\mathcal{B}_{11}^{(a_2)} = \mathcal{A}_{11}^{(a_2)} = cs f_1(\mathbf{k}_2)$ is given by Eq. (A10). Obviously, the dynamical information of the source in Eq. (C9) is described by

$$\sum_{(i,i')} \mathcal{J}_{ii'}^{(11)} \langle a_1^\dagger a_2 \tilde{\sigma}_{ii'} \rangle = -\beta_1 \langle a_1^\dagger a_2 \tilde{\sigma}_{11} \rangle + \alpha_4 \langle a_1^\dagger a_2 \tilde{\sigma}_{33} \rangle + \alpha_3 \langle a_1^\dagger a_2 \tilde{\sigma}_{44} \rangle. \tag{C10}$$

2. Proof of the factorizations

Taking the correlator $\langle a^\dagger b \tilde{\sigma}_{rs} \rangle$ as an example, let us first explore the relation between the second-order correlators and first-order correlators. From Eq. (C5), it is straightforward to write the equations of motion for the second-order correlator $\langle a^\dagger b \tilde{\sigma}_{rs} \rangle$ and its coupled terms

$$\frac{d}{dt} \langle a^\dagger b \tilde{\sigma}_{rs} \rangle = -\mathcal{K}_{rs}^{(1,0,1,0)} \langle a^\dagger b \tilde{\sigma}_{rs} \rangle + \sum_{(i,i')} \mathcal{J}_{ii'}^{(rs)} \langle a^\dagger b \tilde{\sigma}_{ii'} \rangle - \sqrt{\mu\kappa\gamma} \left(\sum_j \mathcal{B}_{rj}^{(a)*} \langle b \tilde{\sigma}_{js} \rangle + \sum_j \mathcal{B}_{sj}^{(b)} \langle a^\dagger \tilde{\sigma}_{rj} \rangle \right), \tag{C11a}$$

$$\frac{d}{dt} \langle a^\dagger \tilde{\sigma}_{rj} \rangle = -\mathcal{K}_{rj}^{(1,0,0,0)} \langle a^\dagger \tilde{\sigma}_{rj} \rangle + \sum_{(i,i')} \mathcal{J}_{ii'}^{(rj)} \langle a^\dagger \tilde{\sigma}_{ii'} \rangle - \sqrt{\mu\kappa\gamma} \sum_{j'} \mathcal{B}_{rj'}^{(a)*} \langle \tilde{\sigma}_{j'j}(t) \rangle, \tag{C11b}$$

$$\frac{d}{dt} \langle b \tilde{\sigma}_{js} \rangle = -\mathcal{K}_{js}^{(0,0,1,0)} \langle b \tilde{\sigma}_{js} \rangle + \sum_{(i,i')} \mathcal{J}_{ii'}^{(js)} \langle b \tilde{\sigma}_{ii'} \rangle - \sqrt{\mu\kappa\gamma} \sum_{j'} \mathcal{B}_{sj'}^{(b)} \langle \tilde{\sigma}_{jj'}(t) \rangle. \tag{C11c}$$

Here we should note that, in the limit of large passband width ($\kappa \gg \gamma$), the characteristic timescale of the correlators is κ^{-1}, which is small compared with the atomic evolution time γ^{-1} [71,72]. On this timescale, we can ignore the small contributions that are of the order of γ compared with κ, i.e., the second term in the right-hand side of Eq. (C5) and that in Eqs. (C11a)–(C11c), and use the steady-state approximation only for the atomic variables in the last term of Eqs. (C11b) and (C11c), i.e., $\langle \tilde{\sigma}_{jj'}(t) \rangle \approx \langle \tilde{\sigma}_{jj'} \rangle = \tilde{\rho}_{jj}$ for $j = j'$ and $\langle \tilde{\sigma}_{jj'} \rangle = \rho_{j'j} = 0$ for $j \neq j'$, to remove the summation symbol. In addition, the initial state of the system is $\tilde{\rho}_{S,ab}(t=0) = \tilde{\rho}_S \otimes |0_a, 0_b\rangle\langle 0_a, 0_b|$ without any photon being prepared in the target cavities, which suggests that the initial values of all the correlators are zero (except for zeroth-order correlators, i.e., the atomic populations). Therefore we can conclude that all the correlators and their equations of motion can be decomposed according to the steady-state populations $\{\langle \tilde{\sigma}_{jj} \rangle\}$ without constant term, i.e., we have the decomposition $\langle a^{\dagger m} b^{\dagger p} b^q a^n \tilde{\sigma}_{rs} \rangle = \sum_j \langle \tilde{\sigma}_{jj} \rangle \langle a^{\dagger m} b^{\dagger p} b^q a^n \tilde{\sigma}_{rs} \rangle_j$. Specifically, the reduced correlators $\langle b \tilde{\sigma}_{js} \rangle_j$, $\langle a^\dagger \tilde{\sigma}_{rj} \rangle_j$, and $\langle a^\dagger b \tilde{\sigma}_{rs} \rangle_j$ are determined by

$$\langle b \tilde{\sigma}_{js} \rangle = \sum_{j'} \langle \tilde{\sigma}_{j'j'} \rangle \langle b \tilde{\sigma}_{js} \rangle_{j'} = \langle \tilde{\sigma}_{jj} \rangle \langle b \tilde{\sigma}_{js} \rangle_j, \tag{C12a}$$

$$\langle a^\dagger \tilde{\sigma}_{rj} \rangle = \sum_{j'} \langle \tilde{\sigma}_{j'j'} \rangle \langle a^\dagger \tilde{\sigma}_{rj} \rangle_{j'} = \langle \tilde{\sigma}_{jj} \rangle \langle a^\dagger \tilde{\sigma}_{rj} \rangle_j, \tag{C12b}$$

$$\langle a^\dagger b \tilde{\sigma}_{rs} \rangle = \sum_{j'} \langle \tilde{\sigma}_{j'j'} \rangle \langle a^\dagger b \tilde{\sigma}_{rs} \rangle_{j'}. \tag{C12c}$$

In Eqs. (C12a) and (C12b), the second equalities are based on the fact that the first-order correlators $\langle b\tilde{\sigma}_{js}\rangle$ and $\langle a^{\dagger}\tilde{\sigma}_{rj}\rangle$ are only proportional to the single steady-state population $\langle\tilde{\sigma}_{jj}\rangle$ [see Eqs. (C11b) and (C11c)). Thus the equations of motion for the reduced correlators $\langle b\tilde{\sigma}_{js}\rangle_{j}$ and $\langle a^{\dagger}\tilde{\sigma}_{rj}\rangle_{j}$ can be obtained mathematically from Eqs. (C11b), and (C11c) by setting $\langle\tilde{\sigma}_{jj}\rangle = 1$ and $\langle\tilde{\sigma}_{j'j'}\rangle = 0$ $(j' \neq j)$ to remove the summation symbols, which turn out to be

$$\frac{d}{dt}\langle a^{\dagger}\tilde{\sigma}_{rj}\rangle_{j} \approx -\mathcal{K}_{rj}^{(1,0,0,0)}\langle a^{\dagger}\tilde{\sigma}_{rj}\rangle_{j} - \sqrt{\mu\kappa\gamma}\mathcal{B}_{rj}^{(a)*}, \tag{C13a}$$

$$\frac{d}{dt}\langle b\tilde{\sigma}_{js}\rangle_{j} \approx -\mathcal{K}_{js}^{(0,0,1,0)}\langle b\tilde{\sigma}_{js}\rangle_{j} - \sqrt{\mu\kappa\gamma}\mathcal{B}_{sj}^{(b)}. \tag{C13b}$$

Comparing Eq. (C11a) with Eqs. (C13a) and (C13b), it is not difficult to find that the relation between these equations seems to be revealed by calculating the evolution of the product $\langle a^{\dagger}\tilde{\sigma}_{rj}\rangle_{j}\langle b\tilde{\sigma}_{js}\rangle_{j}$, which turns out to be

$$\frac{d}{dt}(\langle a^{\dagger}\tilde{\sigma}_{rj}\rangle_{j}\langle b\tilde{\sigma}_{js}\rangle_{j}) = \left(\frac{d}{dt}\langle a^{\dagger}\tilde{\sigma}_{rj}\rangle_{j}\right)\langle b\tilde{\sigma}_{js}\rangle_{j} + \langle a^{\dagger}\tilde{\sigma}_{rj}\rangle_{j}\left(\frac{d}{dt}\langle b\tilde{\sigma}_{js}\rangle_{j}\right)$$

$$\approx -\mathcal{K}_{rs}^{(1,0,1,0)}(\langle a^{\dagger}\tilde{\sigma}_{rj}\rangle_{j}\langle b\tilde{\sigma}_{js}\rangle_{j}) - \sqrt{\mu\kappa\gamma}(\mathcal{B}_{rj}^{(a)*}\langle b\tilde{\sigma}_{js}\rangle_{j} + \mathcal{B}_{sj}^{(b)}\langle a^{\dagger}\tilde{\sigma}_{rj}\rangle_{j}), \tag{C14}$$

where we have used the relation $\mathcal{K}_{rj}^{(1,0,0,0)} + \mathcal{K}_{js}^{(0,0,1,0)} = \mathcal{K}_{rs}^{(1,0,1,0)}$. Because of the decomposability of Eq. (C5) for arbitrary population distributions $\{\langle\tilde{\sigma}_{11}\rangle, \langle\tilde{\sigma}_{22}\rangle, \ldots, \langle\tilde{\sigma}_{88}\rangle\}$, the equation of motion for the reduced correlator $\langle a^{\dagger m}b^{\dagger p}b^{q}a^{n}\tilde{\sigma}_{rs}\rangle_{j}$ can be obtained mathematically by setting $\langle\tilde{\sigma}_{jj}\rangle = 1$ and $\langle\tilde{\sigma}_{j'j'}\rangle = 0$ $(j' \neq j)$ in Eq. (C5). Accordingly, the equation of motion for the reduced second-order correlator $\langle a^{\dagger}b\tilde{\sigma}_{rs}\rangle_{j}$ is obtained by setting $\langle\tilde{\sigma}_{jj}\rangle = 1$ and $\langle\tilde{\sigma}_{j'j'}\rangle = 0$ $(j' \neq j)$ and ignoring the terms of atomic decay rates in Eq. (C11a), which takes the form

$$\frac{d}{dt}\langle a^{\dagger}b\tilde{\sigma}_{rs}\rangle_{j} \approx -\mathcal{K}_{rs}^{(1,0,1,0)}\langle a^{\dagger}b\tilde{\sigma}_{rs}\rangle_{j} - \sqrt{\mu\kappa\gamma}(\mathcal{B}_{rj}^{(a)*}\langle b\tilde{\sigma}_{js}\rangle_{j} + \mathcal{B}_{sj}^{(b)}\langle a^{\dagger}\tilde{\sigma}_{rj}\rangle_{j}). \tag{C15}$$

Obviously, the dynamical evolution described by Eq. (C15) is consistent with that described by Eq. (C14). Given the fact that the initial values of all the correlators are zero, so far, we have found the factorization

$$\langle a^{\dagger}b\tilde{\sigma}_{rs}\rangle_{j} = \langle a^{\dagger}\tilde{\sigma}_{rj}\rangle_{j}\langle b\tilde{\sigma}_{js}\rangle_{j}. \tag{C16}$$

The factorization for other second-order correlators can be derived similarly.

We now proceed to examine the higher-order correlators. Due to the recurrence relation between the $(m + n + p + q)$th-order and the $(m + n + p + q - 1)$th-order correlators, inspired by the decomposition for the second-order correlators obtained in the above, we may as well assume that the $(m + n + p + q - 1)$th-order correlators satisfy the factorizations

$$\langle a^{\dagger m-1}b^{\dagger p}b^{q}a^{n}\tilde{\sigma}_{rs}\rangle_{j} = \langle a^{\dagger m-1}b^{\dagger p}\tilde{\sigma}_{rj}\rangle_{j}\langle a^{n}b^{q}\tilde{\sigma}_{js}\rangle_{j}, \tag{C17a}$$

$$\langle a^{\dagger m}b^{\dagger p-1}b^{q}a^{n}\tilde{\sigma}_{rs}\rangle_{j} = \langle a^{\dagger m}b^{\dagger p-1}\tilde{\sigma}_{rj}\rangle_{j}\langle a^{n}b^{q}\tilde{\sigma}_{js}\rangle_{j}, \tag{C17b}$$

$$\langle a^{\dagger m}b^{\dagger p}b^{q}a^{n-1}\tilde{\sigma}_{rs}\rangle_{j} = \langle a^{\dagger m}b^{\dagger p}\tilde{\sigma}_{rj}\rangle_{j}\langle a^{n-1}b^{q}\tilde{\sigma}_{js}\rangle_{j}, \tag{C17c}$$

$$\langle a^{\dagger m}b^{\dagger p}b^{q-1}a^{n}\tilde{\sigma}_{rs}\rangle_{j} = \langle a^{\dagger m}b^{\dagger p}\tilde{\sigma}_{rj}\rangle_{j}\langle a^{n}b^{q-1}\tilde{\sigma}_{js}\rangle_{j}. \tag{C17d}$$

As mentioned in the above, because of the decomposability of Eq. (C5) for arbitrary population distributions, the equations of motion for all the reduced correlators reduced by $\langle\tilde{\sigma}_{jj}\rangle$ can be obtained mathematically from Eq. (C5) by setting $\langle\tilde{\sigma}_{jj}\rangle = 1$ and $\langle\tilde{\sigma}_{j'j'}\rangle = 0$ $(j' \neq j)$ to replace the coupled lower-order correlators with the corresponding reduced correlators. Thus the relation between the $(m + n + p + q)$th-order and the $(m + n + p + q - 1)$th-order reduced correlators can be obtained through the equations

$$\left(\frac{d}{dt}\langle a^{\dagger m}b^{\dagger p}\tilde{\sigma}_{rj}\rangle_{j}\right)\langle a^{n}b^{q}\tilde{\sigma}_{js}\rangle_{j} \approx -\mathcal{K}_{rj}^{(m,p,0,0)}(\langle a^{\dagger m}b^{\dagger p}\tilde{\sigma}_{rj}\rangle_{j}\langle a^{n}b^{q}\tilde{\sigma}_{js}\rangle_{j})$$

$$- \sqrt{\mu\kappa\gamma}\left[m\sum_{j'}\mathcal{B}_{rj'}^{(a)*}(\langle a^{\dagger m-1}b^{\dagger p}\tilde{\sigma}_{j'j}\rangle_{j}\langle a^{n}b^{q}\tilde{\sigma}_{js}\rangle_{j})\right]$$

$$- \sqrt{\mu\kappa\gamma}\left[p\sum_{j'}\mathcal{B}_{rj'}^{(b)*}(\langle a^{\dagger m}b^{\dagger p-1}\tilde{\sigma}_{j'j}\rangle_{j}\langle a^{n}b^{q}\tilde{\sigma}_{js}\rangle_{j})\right], \tag{C18a}$$

$$\left(\frac{d}{dt}\langle a^{n}b^{q}\tilde{\sigma}_{js}\rangle_{j}\right)\langle a^{\dagger m}b^{\dagger p}\tilde{\sigma}_{rj}\rangle_{j} \approx -\mathcal{K}_{js}^{(0,0,q,n)}(\langle a^{\dagger m}b^{\dagger p}\tilde{\sigma}_{rj}\rangle_{j}\langle a^{n}b^{q}\tilde{\sigma}_{js}\rangle_{j}) - \sqrt{\mu\kappa\gamma}\left[n\sum_{j'}\mathcal{B}_{sj'}^{(a)}(\langle a^{\dagger m}b^{\dagger p}\tilde{\sigma}_{rj}\rangle_{j}\langle a^{n-1}b^{q}\tilde{\sigma}_{jj'}\rangle_{j})\right]$$

$$- \sqrt{\mu\kappa\gamma}\left[q\sum_{j'}\mathcal{B}_{sj'}^{(b)}(\langle a^{\dagger m}b^{\dagger p}\tilde{\sigma}_{rj}\rangle_{j}\langle a^{n}b^{q-1}\tilde{\sigma}_{jj'}\rangle_{j})\right]. \tag{C18b}$$

Substituting Eqs. (C17a)–(C17d) into Eqs. (C18a) and (C18b), and adding Eqs. (C18a) and (C18b) together, we find

$$\frac{d}{dt}(\langle a^{\dagger m} b^{\dagger p} \tilde{\sigma}_{rj} \rangle_j \langle a^n b^q \tilde{\sigma}_{js} \rangle_j) = \frac{d}{dt} \langle a^{\dagger m} b^{\dagger p} b^q a^n \tilde{\sigma}_{rs} \rangle_j, \tag{C19}$$

where we have used the relation $\mathcal{K}_{rj}^{(m,p,0,0)} + \mathcal{K}_{js}^{(0,0,q,n)} = \mathcal{K}_{rs}^{(m,p,q,n)}$. Eq. (C19) indicates that the common equation of motion and the common initial value of $\langle a^{\dagger m} b^{\dagger p} b^q a^n \tilde{\sigma}_{rs} \rangle_j$ and $\langle a^{\dagger m} b^{\dagger p} \tilde{\sigma}_{rj} \rangle_j \langle a^n b^q \tilde{\sigma}_{js} \rangle_j$ ensure that the $(m + n + p + q)$th-order reduced correlator also satisfies the factorization

$$\langle a^{\dagger m} b^{\dagger p} b^q a^n \tilde{\sigma}_{rs} \rangle_j = \langle a^{\dagger m} b^{\dagger p} \tilde{\sigma}_{rj} \rangle_j \langle a^n b^q \tilde{\sigma}_{js} \rangle_j \tag{C20}$$

if the factorization holds for the $(m + n + p + q - 1)$th-order correlators, i.e., Eqs. (C17a)–(C17d). Obviously, Eq. (C20) is the factorization in Eq. (18) in the diagonalized atomic representation.

Based on the above two steps, we have proved the factorization (18) for all the $(m + n + p + q)$th-order correlators with $(m + n + p + q) \geqslant 2$ in the diagonalized atomic representation. Similarly, the factorization for single-mode correlators can be also obtained through the same procedure, and takes the form

$$\langle a^{\dagger m} a^n \tilde{\sigma}_{rs} \rangle_j = \langle a^{\dagger m} \tilde{\sigma}_{rj} \rangle_j \langle a^n \tilde{\sigma}_{js} \rangle_j. \tag{C21}$$

Physically, the factorizations in Eqs. (C20) and (C21) suggest that, in the limit of large passband width, the emissions triggered by a single independent population can be addressable individually, and some reduced correlators, such as $\langle a^n b^q \tilde{\sigma}_{js} \rangle_j$, play the role of probability amplitudes. Based on these factorizations and ignoring higher-order terms in the truncated reduced density matrix elements, we can formally rewrite the approximate truncated reduced density operator of the atom-photon combined system in Eqs. (16a) and (16b) in the language of the probability amplitudes.

APPENDIX D: ANALYTICAL EXPRESSIONS OF THE PROBABILITY AMPLITUDES IN EQUATIONS (20a), (20b), (22a), AND (22b)

As an example, in this Appendix, we select the two-photon cascaded emissions for the two-mode fields (a_1, a_2) only in a single cascaded emission group to present the analytical expressions of the probability amplitudes in Eqs. (20b) and (22b). The analytical expressions of the other wave functions in Eqs. (20b) and (22b) can be also given similarly. Finally, we briefly present the single-mode probability amplitudes.

For the two-mode cavity fields (a_1, a_2) in the diagonalized atomic representation $\{|\tilde{j}\rangle\}$ $(j \in \{1, 2, \ldots, 8\})$, the wave function of the two-photon cascaded emissions triggered by the diagonalized atomic state $|\tilde{1}\rangle$, for example, takes the form

$$\begin{aligned}
\big|\tilde{\Psi}_{S,a_1 a_2}^{(1)}\big\rangle = {} & \big|\tilde{1}, 0_{a_1}, 0_{a_2}\big\rangle + \tilde{\mathcal{C}}_{1,0_{a_1},1_{a_2}}^{(1)} \big|\tilde{1}, 0_{a_1}, 1_{a_2}\big\rangle \\
& + \tilde{\mathcal{C}}_{2,1_{a_1},0_{a_2}}^{(1)} \big|\tilde{2}, 1_{a_1}, 0_{a_2}\big\rangle + \tilde{\mathcal{C}}_{3,1_{a_1},0_{a_2}}^{(1)} \big|\tilde{3}, 1_{a_1}, 0_{a_2}\big\rangle + \tilde{\mathcal{C}}_{4,1_{a_1},0_{a_2}}^{(1)} \big|\tilde{4}, 1_{a_1}, 0_{a_2}\big\rangle \\
& + \tilde{\mathcal{C}}_{2,1_{a_1},1_{a_2}}^{(1)} \big|\tilde{2}, 1_{a_1}, 1_{a_2}\big\rangle + \tilde{\mathcal{C}}_{3,1_{a_1},1_{a_2}}^{(1)} \big|\tilde{3}, 1_{a_1}, 1_{a_2}\big\rangle + \tilde{\mathcal{C}}_{4,1_{a_1},1_{a_2}}^{(1)} \big|\tilde{4}, 1_{a_1}, 1_{a_2}\big\rangle,
\end{aligned} \tag{D1}$$

where the steady-state probability amplitudes in Eq. (D1) are given by the steady-state solutions of the corresponding reduced correlators as

$$\tilde{\mathcal{C}}_{1,0_{a_1},1_{a_2}}^{(1)} = \langle a_2 \tilde{\sigma}_{11} \rangle_1 = \frac{\sqrt{\mu \kappa \gamma} \mathcal{B}_{11}^{(a_2)}}{\frac{\kappa}{2} + i\delta_2}, \qquad \tilde{\mathcal{C}}_{2,1_{a_1},0_{a_2}}^{(1)} = \langle a_1 \tilde{\sigma}_{12} \rangle_1 = \frac{\sqrt{\mu \kappa \gamma} \mathcal{B}_{21}^{(a_1)}}{\frac{\kappa}{2} + i(\delta_1 + \tilde{\Omega}_{21})},$$

$$\tilde{\mathcal{C}}_{3,1_{a_1},0_{a_2}}^{(1)} = \langle a_1 \tilde{\sigma}_{13} \rangle_1 = \frac{\sqrt{\mu \kappa \gamma} \mathcal{B}_{31}^{(a_1)}}{\frac{\kappa}{2} + i(\delta_1 + \tilde{\Omega}_{31})}, \qquad \tilde{\mathcal{C}}_{4,1_{a_1},0_{a_2}}^{(1)} = \langle a_1 \tilde{\sigma}_{14} \rangle_1 = \frac{\sqrt{\mu \kappa \gamma} \mathcal{B}_{41}^{(a_1)}}{\frac{\kappa}{2} + i(\delta_1 + \tilde{\Omega}_{41})},$$

$$\begin{aligned}
\tilde{\mathcal{C}}_{2,1_{a_1},1_{a_2}}^{(1)} &= \langle a_1 a_2 \tilde{\sigma}_{12} \rangle_1 \\
&= \frac{\sqrt{\mu \kappa \gamma}}{\kappa + i(\delta_{12} + \tilde{\Omega}_{21})} \big(\mathcal{B}_{21}^{(a_1)} \tilde{\mathcal{C}}_{1,0_{a_1},1_{a_2}}^{(1)} + \mathcal{B}_{22}^{(a_2)} \tilde{\mathcal{C}}_{2,1_{a_1},0_{a_2}}^{(1)} + \mathcal{B}_{23}^{(a_2)} \tilde{\mathcal{C}}_{3,1_{a_1},0_{a_2}}^{(1)} + \mathcal{B}_{24}^{(a_2)} \tilde{\mathcal{C}}_{4,1_{a_1},0_{a_2}}^{(1)} \big),
\end{aligned}$$

$$\begin{aligned}
\tilde{\mathcal{C}}_{3,1_{a_1},1_{a_2}}^{(1)} &= \langle a_1 a_2 \tilde{\sigma}_{13} \rangle_1 \\
&= \frac{\sqrt{\mu \kappa \gamma}}{\kappa + i(\delta_{12} + \tilde{\Omega}_{31})} \big(\mathcal{B}_{31}^{(a_1)} \tilde{\mathcal{C}}_{1,0_{a_1},1_{a_2}}^{(1)} + \mathcal{B}_{32}^{(a_2)} \tilde{\mathcal{C}}_{2,1_{a_1},0_{a_2}}^{(1)} + \mathcal{B}_{34}^{(a_2)} \tilde{\mathcal{C}}_{4,1_{a_1},0_{a_2}}^{(1)} \big),
\end{aligned}$$

$$\begin{aligned}
\tilde{\mathcal{C}}_{4,1_{a_1},1_{a_2}}^{(1)} &= \langle a_1 a_2 \tilde{\sigma}_{14} \rangle_1 \\
&= \frac{\sqrt{\mu \kappa \gamma}}{\kappa + i(\delta_{12} + \tilde{\Omega}_{41})} \big(\mathcal{B}_{41}^{(a_1)} \tilde{\mathcal{C}}_{1,0_{a_1},1_{a_2}}^{(1)} + \mathcal{B}_{42}^{(a_2)} \tilde{\mathcal{C}}_{2,1_{a_1},0_{a_2}}^{(1)} + \mathcal{B}_{43}^{(a_2)} \tilde{\mathcal{C}}_{3,1_{a_1},0_{a_2}}^{(1)} + \mathcal{B}_{44}^{(a_2)} \tilde{\mathcal{C}}_{4,1_{a_1},0_{a_2}}^{(1)} \big),
\end{aligned} \tag{D2}$$

where $\delta_{12} = \delta_1 + \delta_2$ and $\tilde{\Omega}_{jj'} = \tilde{\Omega}_j - \tilde{\Omega}_{j'}$. Obviously, these expressions of coherent superpositions show that multichannel interferences are established if these channels are terminated by a common target atomic state and triggered by a common initial atomic state. The explicit expressions of the other two-mode wave functions in Eq. (20b) can be also given formally by the corresponding steady-state reduced correlators.

The influence of the steady-state atomic coherent effects ρ_{24}, ρ_{42}, ρ_{67}, and ρ_{76} on the directionality of radiation in our system can be highlighted by transforming the diagonalized steady-state density operator $\tilde{\rho}_{S,ab}$ in Eq. (19b) back to the original dressed-state representation $\{|k\rangle\}$ ($k \in \{1, 2, \ldots, 8\}$) via Eqs. (13) and (14). In order to obtain a transparent form of the dressed-state probability amplitudes similar to Eq. (D2), we can further ignore the small energy-level shifts $\delta\tilde{\Omega}_j$ with respect to κ. In this case, $\tilde{\Omega}_j \approx \tilde{\Omega}_j^{(0)} = \Omega_j^{(0)}$, and one can obtain the wave functions $|\Psi_{S,a_1a_2}^{(k)}\rangle$ in the dressed-state representation in Eq. (22b). For example, the wave function $|\Psi_{S,a_1a_2}^{(2)}\rangle$, which describes the two-photon cascaded emissions triggered by the dressed state $|2\rangle$, takes the form

$$
\begin{aligned}
\left|\Psi_{S,a_1a_2}^{(2)}\right\rangle = &\left|2, 0_{a_1}, 0_{a_2}\right\rangle \\
&+ \mathcal{C}_{2,0_{a_1},1_{a_2}}^{(2)}\left|2, 0_{a_1}, 1_{a_2}\right\rangle + \mathcal{C}_{5,1_{a_1},0_{a_2}}^{(2)}\left|5, 1_{a_1}, 0_{a_2}\right\rangle \\
&+ \mathcal{C}_{6,1_{a_1},0_{a_2}}^{(2)}\left|6, 1_{a_1}, 0_{a_2}\right\rangle + \mathcal{C}_{5,1_{a_1},1_{a_2}}^{(2)}\left|5, 1_{a_1}, 1_{a_2}\right\rangle + \mathcal{C}_{6,1_{a_1},1_{a_2}}^{(2)}\left|6, 1_{a_1}, 1_{a_2}\right\rangle,
\end{aligned}
\tag{D3}
$$

where the analytical expressions of the steady-state probability amplitudes are given by

$$
\mathcal{C}_{2,0_{a_1},1_{a_2}}^{(2)} = \frac{\sqrt{\mu\kappa\gamma}\,\mathcal{A}_{22}^{(a_2)}}{\frac{\kappa}{2} + i\delta_2},
$$

$$
\mathcal{C}_{5,1_{a_1},0_{a_2}}^{(2)} = \frac{\sqrt{\mu\kappa\gamma}\,\mathcal{A}_{52}^{(a_1)}}{\frac{\kappa}{2} + i\left(\delta_1 + \Omega_{52}^{(0)}\right)}, \qquad \mathcal{C}_{6,1_{a_1},0_{a_2}}^{(2)} = \frac{\sqrt{\mu\kappa\gamma}\,\mathcal{A}_{62}^{(a_1)}}{\frac{\kappa}{2} + i\left(\delta_1 + \Omega_{62}^{(0)}\right)},
$$

$$
\mathcal{C}_{5,1_{a_1},1_{a_2}}^{(2)} = \frac{\sqrt{\mu\kappa\gamma}}{\kappa + i\left(\delta_{12} + \Omega_{52}^{(0)}\right)}\left(\mathcal{A}_{52}^{(a_1)}\mathcal{C}_{2,0_{a_1},1_{a_2}}^{(2)} + \mathcal{A}_{56}^{(a_2)}\mathcal{C}_{6,1_{a_1},0_{a_2}}^{(2)}\right),
$$

$$
\mathcal{C}_{6,1_{a_1},1_{a_2}}^{(2)} = \frac{\sqrt{\mu\kappa\gamma}}{\kappa + i\left(\delta_{12} + \Omega_{62}^{(0)}\right)}\left(\mathcal{A}_{62}^{(a_1)}\mathcal{C}_{2,0_{a_1},1_{a_2}}^{(2)} + \mathcal{A}_{65}^{(a_2)}\mathcal{C}_{5,1_{a_1},0_{a_2}}^{(2)}\right),
\tag{D4}
$$

with $\Omega_{kk'}^{(0)} = \Omega_k^{(0)} - \Omega_{k'}^{(0)}$. The explicit expressions of the other two-mode wave functions in Eq. (22b) can be also given similarly. The main physical mechanism can be revealed with the help of the probability amplitudes.

For the sake of completeness, we briefly present an example of the analytical expressions for the single-mode probability amplitudes in Eq. (22a), After solving the single-mode correlators in the diagonalized atomic representation for the system composed of the source plus the three-body collective mode a_1, for example, and transforming back to the dressed-state representation, the cascaded emissions triggered by the dressed state $|1\rangle$ can be described by the following wave function

$$
\begin{aligned}
\left|\Psi_{S,a_1}^{(1)}\right\rangle = &\left|1, 0_{a_1}\right\rangle \\
&+ \mathcal{C}_{2,1_{a_1}}^{(1)}\left|2, 1_{a_1}\right\rangle + \mathcal{C}_{3,1_{a_1}}^{(1)}\left|3, 1_{a_1}\right\rangle + \mathcal{C}_{4,1_{a_1}}^{(1)}\left|4, 1_{a_1}\right\rangle \\
&+ \mathcal{C}_{5,2_{a_1}}^{(1)}\left|5, 2_{a_1}\right\rangle + \mathcal{C}_{6,2_{a_1}}^{(1)}\left|6, 2_{a_1}\right\rangle + \mathcal{C}_{7,2_{a_1}}^{(1)}\left|7, 2_{a_1}\right\rangle,
\end{aligned}
\tag{D5}
$$

where the analytical expressions of the steady-state probability amplitudes are given by

$$
\mathcal{C}_{2,1_{a_1}}^{(1)} = \frac{\sqrt{\mu\kappa\gamma}\,\mathcal{A}_{21}^{(a_1)}}{\frac{\kappa}{2} + i\left(\delta_1 + \Omega_{21}^{(0)}\right)},
$$

$$
\mathcal{C}_{3,1_{a_1}}^{(1)} = \frac{\sqrt{\mu\kappa\gamma}\,\mathcal{A}_{31}^{(a_1)}}{\frac{\kappa}{2} + i\left(\delta_1 + \Omega_{31}^{(0)}\right)}, \qquad \mathcal{C}_{4,1_{a_1}}^{(1)} = \frac{\sqrt{\mu\kappa\gamma}\,\mathcal{A}_{41}^{(a_1)}}{\frac{\kappa}{2} + i\left(\delta_1 + \Omega_{41}^{(0)}\right)},
$$

$$
\mathcal{C}_{5,2_{a_1}}^{(1)} = \frac{\sqrt{2\mu\kappa\gamma}}{\kappa + i\left(2\delta_1 + \Omega_{51}^{(0)}\right)}\left(\mathcal{A}_{52}^{(a_1)}\mathcal{C}_{2,1_{a_1}}^{(1)} + \mathcal{A}_{53}^{(a_1)}\mathcal{C}_{3,1_{a_1}}^{(1)}\right),
$$

$$
\mathcal{C}_{6,2_{a_1}}^{(1)} = \frac{\sqrt{2\mu\kappa\gamma}}{\kappa + i\left(2\delta_1 + \Omega_{61}^{(0)}\right)}\left(\mathcal{A}_{62}^{(a_1)}\mathcal{C}_{2,1_{a_1}}^{(1)} + \mathcal{A}_{64}^{(a_1)}\mathcal{C}_{4,1_{a_1}}^{(1)}\right),
$$

$$
\mathcal{C}_{7,2_{a_1}}^{(1)} = \frac{\sqrt{2\mu\kappa\gamma}}{\kappa + i\left(2\delta_1 + \Omega_{71}^{(0)}\right)}\left(\mathcal{A}_{73}^{(a_1)}\mathcal{C}_{3,1_{a_1}}^{(1)} + \mathcal{A}_{74}^{(a_1)}\mathcal{C}_{4,1_{a_1}}^{(1)}\right).
\tag{D6}
$$

APPENDIX E: FULL SOLUTIONS OF THE FREQUENCY-RESOLVED CORRELATION FUNCTIONS IN SECTION IV

In this Appendix, we present the full analytical expressions of the frequency-resolved correlation functions plotted in Figs. 5(a), 7(b), and 12(a). In the full solutions, the contributions of all the populations $(\rho_{11}, \rho_{22}, \ldots, \rho_{88})$ and the atomic coherences $(\rho_{24}, \rho_{42}, \rho_{67}, \rho_{76})$ are considered, giving rise to the results in Figs. 5(a), 7(b), and 12(a) without any additional approximations.

1. Full solution of the frequency-resolved intensity-intensity correlation function

The frequency-resolved intensity-intensity correlation function $G^{(2)}_{a_1 a_3}$ plotted in Fig. 5(a) involves all the two-photon probabilities triggered by the dressed states $\{|k\rangle\}$ ($k \in \{1, 2, \ldots, 8\}$) and all the quantum interferences of the two-photon cascaded channels from the correlated atomic states $\{|2\rangle, |4\rangle\}$ and $\{|6\rangle, |7\rangle\}$. Based on the analytical approach proposed in Sec. III, the full explicit expression of $G^{(2)}_{a_1 a_3}$ is calculated as

$$G^{(2)}_{a_1 a_3} = \sum_{k=1}^{8} \left(G^{(2)}_{a_1 a_3} \right)_{kk} + \left(G^{(2)}_{a_1 a_3} \right)_{24} + \left(G^{(2)}_{a_1 a_3} \right)_{42} + \left(G^{(2)}_{a_1 a_3} \right)_{67} + \left(G^{(2)}_{a_1 a_3} \right)_{76}, \tag{E1}$$

where the probability components are expressed as

$$\left(G^{(2)}_{a_1 a_3} \right)_{kk'} = \rho_{k'k} \sum_j \mathcal{C}^{(k)*}_{j, 1_{a_1}, 1_{a_3}} \mathcal{C}^{(k')}_{j, 1_{a_1}, 1_{a_3}}, \quad \begin{cases} j = 1, & \text{for } (k, k') = (1, 1), \\ j = 2, & \text{for } (k, k') = (2, 2), \\ j = 8, & \text{for } (k, k') = (8, 8), \\ j = 2, 3, 4, & \text{for } (k, k') = (3, 3), (4, 4), \\ j = 5, 6, & \text{for } (k, k') = (5, 5), (6, 6), \\ j = 7, & \text{for } (k, k') = (7, 7), \\ j = 2, & \text{for } (k, k') = (2, 4), (4, 2), \\ j = 5, 6, & \text{for } (k, k') = (6, 7), (7, 6). \end{cases} \tag{E2}$$

In Eq. (E2), the components indicated by $k = k'$ and $k \neq k'$ arise from the population ρ_{kk} and the atomic coherence $\rho_{kk'}$, respectively. The probability components, $(G^{(2)}_{a_1 a_3})_{22}$, $(G^{(2)}_{a_1 a_3})_{24} + (G^{(2)}_{a_1 a_3})_{42}$, and the term $(G^{(2)}_{a_1 a_3})_{44}$ for $j = 2$ correspond to the components $\mathcal{P}^{(22)}$, $\sum_{j,j'=1,2} \mathcal{P}^{(24)}_{jj'}$, and $\mathcal{P}^{(44)}$ in Eq. (25), respectively.

2. Full solution of the frequency-resolved intensity-field correlation function

Next, we present the full analytical expression of the frequency-resolved intensity-field correlation function $G^{(1.5)}_{a_1 a_2}$ plotted in Fig. 7(b). According to the definition of the intensity-field correlation function for the photon pair (a_1, a_2), i.e., $G^{(1.5)}_{a_1 a_2} = \langle a_1^\dagger a_2 a_1 \rangle e^{-x} + \langle a_1^\dagger a_2^\dagger a_1 \rangle e^{x}$, the correlator $\mathcal{G}^{(1.5)}_{a_1 a_2} = \langle a_1^\dagger a_2 a_1 \rangle$ is given by

$$\mathcal{G}^{(1.5)}_{a_1 a_2} = \sum_{k=1}^{7} \left(\mathcal{G}^{(1.5)}_{a_1 a_2} \right)_{kk} + \left(\mathcal{G}^{(1.5)}_{a_1 a_2} \right)_{24} + \left(\mathcal{G}^{(1.5)}_{a_1 a_2} \right)_{42} + \left(\mathcal{G}^{(1.5)}_{a_1 a_2} \right)_{67} + \left(\mathcal{G}^{(1.5)}_{a_1 a_2} \right)_{76}, \tag{E3}$$

where the components of the correlator $\mathcal{G}^{(1.5)}_{a_1 a_2}$ are expressed as

$$\left(\mathcal{G}^{(1.5)}_{a_1 a_2} \right)_{kk'} = \rho_{k'k} \sum_j \mathcal{C}^{(k)*}_{j, 1_{a_1}, 0_{a_2}} \mathcal{C}^{(k')}_{j, 1_{a_1}, 1_{a_2}}, \quad \begin{cases} j = 2, 3, 4, & \text{for } (k, k') = (1, 1), \\ j = 5, 6, & \text{for } (k, k') = (2, 2), \\ j = 7, & \text{for } (k, k') = (3, 3), (4, 4), \\ j = 8, & \text{for } (k, k') = (5, 5), (6, 6), (7, 7), \\ j = 5, & \text{for } (k, k') = (2, 4), \\ j = 6, & \text{for } (k, k') = (4, 2), \\ j = 8, & \text{for } (k, k') = (6, 7), (7, 6). \end{cases} \tag{E4}$$

Thus the total value of $G^{(1.5)}_{a_1 a_2}$ in Fig. 7(b) can be obtained as $G^{(1.5)}_{a_1 a_2} = 2\text{Re}[\mathcal{G}^{(1.5)}_{a_1 a_2}]$. We can find from Eq. (E4) that there is no contribution of the population ρ_{88} in $G^{(1.5)}_{a_1 a_2}$, because the first step of the cascaded transitions triggered by the lowest energy level $|8\rangle$ cannot emit higher-frequency photons into the mode a_1.

3. Full solution of the frequency-resolved anomalous correlation function

Finally, we present the full analytical expression of the frequency-resolved anomalous correlation function $G^{(0,2)}_{a_1 a_3}$ plotted in Fig. 12(a). It is given by

$$G^{(0,2)}_{a_1 a_3} = \sum_{k=1}^{8} \left(G^{(0,2)}_{a_1 a_3} \right)_{kk} + \left(G^{(0,2)}_{a_1 a_3} \right)_{42} + \left(G^{(0,2)}_{a_1 a_3} \right)_{76}, \tag{E5}$$

where the components of the correlation function $G_{a_1 a_3}^{(0,2)}$ are expressed as

$$\left(G_{a_1 a_3}^{(0,2)}\right)_{kk'} = \rho_{kk'} \sum_j \mathcal{C}_{j,1_{a_1},1_{a_3}}^{(k)}, \quad \begin{cases} j = k(= k'), & \text{for } (k, k') = (1, 1), (2, 2), \ldots, (7, 7), (8, 8), \\ j = 2, & \text{for } (k, k') = (4, 2), \\ j = 6, & \text{for } (k, k') = (7, 6). \end{cases} \quad \text{(E6)}$$

From the summation index in Eq. (E6), one can see clearly that only the two-photon probability amplitudes identified by $j = k'$ are chosen by the anomalous correlation function in our system. In other words, it reveals the quantum coherence of the target two-photon state $|j, 1_{a_1}, 1_{a_3}\rangle$ and the initial state $|k', 0_{a_1}, 0_{a_3}\rangle$ with $j = k'$ after detecting a pair of sideband photons.

[1] R. H. Dicke, Phys. Rev. **93**, 99 (1954).
[2] R. H. Lehmberg, Phys. Rev. A **2**, 883 (1970).
[3] D. Pavolini, A. Crubellier, P. Pillet, L. Cabaret, and S. Liberman, Phys. Rev. Lett. **54**, 1917 (1985).
[4] R. G. DeVoe and R. G. Brewer, Phys. Rev. Lett. **76**, 2049 (1996).
[5] J. Eschner, C. Raab, F. Schmidt-Kaler, and R. Blatt, Nature (London) **413**, 495 (2001).
[6] C. Hettich, C. Schmitt, J. Zitzmann, S. Kühn, I. Gerhardt, and V. Sandoghdar, Science **298**, 385 (2002).
[7] M. O. Scully and A. A. Svidzinsky, Science **328**, 1239 (2010).
[8] M. Pleinert, J. von Zanthier, and G. S. Agarwal, Optica **4**, 779 (2017).
[9] S. Mährlein, L. Götzendörfer, K. Günthner, J. Evers, and J. von Zanthier, Phys. Rev. Research **2**, 013278 (2020).
[10] H. H. Jen, M. S. Chang, G. D. Lin, and Y. C. Chen, Phys. Rev. A **101**, 023830 (2020).
[11] Y. X. Zhang, C. Yu, and K. Molmer, Phys. Rev. Research **2**, 013173 (2020).
[12] D. E. Chang, L. Jiang, A. V. Gorshkov, and H. J. Kimble, New J. Phys. **14**, 063003 (2012).
[13] S. D. Jenkins, J. Ruostekoski, N. Papasimakis, S. Savo, and N. I. Zheludev, Phys. Rev. Lett. **119**, 053901 (2017).
[14] P. Lodahl, S. Mahmoodian, S. Stobbe, A. Rauschenbeutel, P. Schneeweiss, J. Volz, H. Pichler, and P. Zoller, Nature (London) **541**, 473 (2017).
[15] A. F. van Loo, A. Fedorov, K. Lalumiére, B. C. Sanders, A. Blais, and A. Wallraff, Science **342**, 1494 (2013).
[16] D. L. Moehring, P. Maunz, S. Olmschenk, K. C. Younge, D. N. Matsukevich, L. M. Duan, and C. Monroe, Nature (London) **449**, 68 (2007).
[17] P. Longo and J. Evers, Phys. Rev. Lett. **112**, 193601 (2014).
[18] D. Bhatti, R. Schneider, S. Oppel, and J. von Zanthier, Phys. Rev. Lett. **120**, 113603 (2018).
[19] S. Oppel, R. Wiegner, G. S. Agarwal, and J. von Zanthier, Phys. Rev. Lett. **113**, 263606 (2014).
[20] A. Mikhalychev, D. Mogilevtsev, G. Ya. Slepyan, I. Karuseichyk, G. Buchs, D. L. Boiko, and A. Boag, Phys. Rev. Appl. **9**, 024021 (2018).
[21] I. Liberal, I. Ederra, and R. W. Ziolkowski, Phys. Rev. A **97**, 053847 (2018).
[22] I. Liberal, I. Ederra, and R. W. Ziolkowski, Photonics **6**, 14 (2019).
[23] Q.-u.-A. Gulfam and Z. Ficek, Phys. Rev. A **94**, 053831 (2016).
[24] Q.-u.-A. Gulfam and Z. Ficek, Phys. Rev. A **98**, 063824 (2018).
[25] A. Piñeiro Orioli and A. M. Rey, Phys. Rev. A **101**, 043816 (2020).
[26] V. Mkhitaryan, L. Meng, A. Marini, and F. J. G. de Abajo, Phys. Rev. Lett. **121**, 163602 (2018).
[27] A. Asenjo-Garcia, M. Moreno-Cardoner, A. Albrecht, H. J. Kimble, and D. E. Chang, Phys. Rev. X **7**, 031024 (2017).
[28] M. Moreno-Cardoner, D. Plankensteiner, L. Ostermann, D. E. Chang, and H. Ritsch, Phys. Rev. A **100**, 023806 (2019).
[29] H. Labuhn, D. Barredo, S. Ravets, S. De Leséléuc, T. Macrì, T. Lahaye, and A. Browaeys, Nature **534**, 667 (2016).
[30] M. Endres, H. Bernien, A. Keesling, H. Levine, E. R. Anschuetz, A. Krajenbrink, C. Senko, V. Vuletic, M. Greiner, and M. D. Lukin, Science **354**, 1024 (2016).
[31] V. E. Lembessis, A. A. Rsheed, O. M. Aldossary, and Z. Ficek, Phys. Rev. A **88**, 053814 (2013).
[32] V. E. Lembessis, A. Lyras, A. A. Rsheed, O. M. Aldossary, and Z. Ficek, Phys. Rev. A **92**, 023850 (2015).
[33] T. J. Arruda, R. Bachelard, J. Weiner, S. Slama, and P. W. Courteille, Phys. Rev. A **101**, 023828 (2020).
[34] S. Wolf, S. Richter, J. von Zanthier, and F. Schmidt-Kaler, Phys. Rev. Lett. **124**, 063603 (2020).
[35] I. Peshko, D. Mogilevtsev, I. Karuseichyk, A. Mikhalychev, A. P. Nizovtsev, G. Ya. Slepyan, and A. Boag, Opt. Express **27**, 029217 (2019).
[36] Z.-a. Peng, G.-q. Yang, Q.-l. Wu, and G.-x. Li, Phys. Rev. A **99**, 033819 (2019).
[37] J. T. Chang, J. Evers, and M. S. Zubairy, Phys. Rev. A **74**, 043820 (2006).
[38] M. Macovei, J. Evers, G. X. Li, and C. H. Keitel, Phys. Rev. Lett. **98**, 043602 (2007).
[39] S. I. Schmid and J. Evers, Phys. Rev. A **81**, 063805 (2010).
[40] A. Ulhaq, S. Weiler, S. M. Ulrich, R. Roßbach, M. Jetter, and P. Michler, Nat. Photon. **6**, 238 (2012).
[41] C. Sánchez Muñoz, E. del Valle, C. Tejedor, and F. P. Laussy, Phys. Rev. A **90**, 052111 (2014).
[42] M. Peiris, B. Petrak, K. Konthasinghe, Y. Yu, Z. C. Niu, and A. Muller, Phys. Rev. B **91**, 195125 (2015).
[43] Y. Nieves and A. Muller, Phys. Rev. B **98**, 165432 (2018).
[44] C. L. Phillips, A. J. Brash, D. P. S. McCutcheon, J. Iles-Smith, E. Clarke, B. Royall, M. S. Skolnick, A. M. Fox, and A. Nazir, Phys. Rev. Lett. **125**, 043603 (2020).
[45] W. Vogel, Phys. Rev. Lett. **67**, 2450 (1991).
[46] W. Vogel, Phys. Rev. A **51**, 4160 (1995).
[47] W. Vogel, Phys. Rev. Lett. **100**, 013605 (2008).
[48] B. Kühn, W. Vogel, M. Mraz, S. Köhnke, and B. Hage, Phys. Rev. Lett. **118**, 153601 (2017).

[49] S. Gerber, D. Rotter, L. Slodicka, J. Eschner, H. J. Carmichael, and R. Blatt, Phys. Rev. Lett. **102**, 183601 (2009).

[50] H. J. Carmichael, H. M. Castro-Beltran, G. T. Foster, and L. A. Orozco, Phys. Rev. Lett. **85**, 1855 (2000).

[51] G. T. Foster, L. A. Orozco, H. M. Castro-Beltran, and H. J. Carmichael, Phys. Rev. Lett. **85**, 3149 (2000).

[52] G. S. Agarwal, Phys. Rev. A **33**, 2472 (1986).

[53] Z. Ficek and R. Tanás, Z. Phys. D **9**, 27 (1988).

[54] J. Gea-Banacloche, M. Mumba, and M. Xiao, Phys. Rev. B **74**, 165330 (2006).

[55] M. Kozub, L. Pawicki, and P. Machnikowski, Phys. Rev. B **86**, 121305(R) (2012).

[56] A. Sitek and P. Machnikowski, Phys. Rev. B **75**, 035328 (2007).

[57] A. Sitek and P. Machnikowski, Phys. Rev. B **80**, 115319 (2009).

[58] W. Abdussalam and P. Machnikowski, Phys. Rev. B **90**, 125307 (2014).

[59] A. F. Alharbi and Z. Ficek, Phys. Rev. A **82**, 054103 (2010).

[60] T. G. Rudolph, Z. Ficek, and B. J. Dalton, Phys. Rev. A **52**, 636 (1995).

[61] E. del Valle, A. Gonzalez-Tudela, F. P. Laussy, C. Tejedor, and M. J. Hartmann, Phys. Rev. Lett. **109**, 183601 (2012).

[62] C. W. Gardiner, Phys. Rev. Lett. **70**, 2269 (1993).

[63] C. W. Gardiner and A. S. Parkins, Phys. Rev. A **50**, 1792 (1994).

[64] H. J. Carmichael, Phys. Rev. Lett. **70**, 2273 (1993).

[65] J. C. López Carreño, C. Sánchez Muñoz, E. del Valle, and F. P. Laussy, Phys. Rev. A **94**, 063826 (2016).

[66] S. C. Azizabadi, N. L. Naumann, M. Katzer, A. Knorr, and A. Carmele, Phys. Rev. A **96**, 023816 (2017).

[67] M. O. Scully and M. S. Zubairy, *Quantum Optics* (Cambridge University Press, Cambridge, UK, 1997).

[68] Z. Ficek and S. Swain, *Quantum Interference and Coherence: Theory and Experiments* (Springer, Berlin, 2004).

[69] H. Pichler, T. Ramos, A. J. Daley, and P. Zoller, Phys. Rev. A **91**, 042116 (2015).

[70] B. R. Mollow, Phys. Rev. **188**, 1969 (1969).

[71] C. A. Schrama, G. Nienhuis, H. A. Dijkerman, C. Steijsiger, and H. G. M. Heideman, Phys. Rev. A **45**, 8045 (1992).

[72] G. Nienhuis, Phys. Rev. A **47**, 510 (1993).

[73] T. K. Mavrogordatos and J. Larson, Phys. Rev. A **101**, 053849 (2020).

[74] M. D. Reid and D. F. Walls, Phys. Rev. A **34**, 1260 (1986).

[75] A. Miranowicz, M. Bartkowiak, X. Wang, Y. X. Liu, and F. Nori, Phys. Rev. A **82**, 013824 (2010).

[76] M. Hillery and M. S. Zubairy, Phys. Rev. Lett. **96**, 050503 (2006).

[77] M. Hillery and M. S. Zubairy, Phys. Rev. A **74**, 032333 (2006).

[78] W. S. Smyth, S. Swain, Z. Ficek, and M. Scott, Phys. Rev. A **57**, 585 (1998).